Image-Guided Surgery: Are We Getting the Most Out of Small-Molecule Prostate-Specific-Membrane-Antigen-Targeted Tracers?

Albertus Wijnand Hensbergen,[†] Danny M. van Willigen,[†] Florian van Beurden,[†,‡] Pim J. van Leeuwen,[‡] Tessa Buckle,[†,‡] Margret Schottelius,[§] Tobias Maurer,[∥] Hans-Jürgen Wester,[#] and Fijs W. B. van Leeuwen*,[†,‡]

[†]Interventional Molecular Imaging Laboratory, Department of Radiology, Leiden University Medical Center, 2333 ZA Leiden, The Netherlands

[‡]Department of Urology, Netherlands Cancer Institute-Antoni van Leeuwenhoek Hospital, 1066 CX Amsterdam, The Netherlands

[§]Translational Radiopharmaceutical Sciences, Department of Nuclear Medicine, Centre Hospitalier Universitaire Vaudois (CHUV) and Department of Oncology, University of Lausanne (UNIL), 1011 Lausanne, Switzerland

[∥]Department of Urology and Martini-Klinik, Universitätsklinikum Hamburg-Eppendorf, 20251 Hamburg, Germany

[#]Pharmazeutische Radiochemie, Technische Universität München, 85748 Garching, Germany

ABSTRACT: Expressed on virtually all prostate cancers and their metastases, the transmembrane protein prostate-specific membrane antigen (PSMA) provides a valuable target for the imaging of prostate cancer. Not only does PSMA provide a target for noninvasive diagnostic imaging, e.g., PSMA-positron emission tomography (PSMA−PET), it can also be used to guide surgical resections of PSMA-positive lesions. The latter characteristic has led to the development of a plethora of PSMA-targeted tracers, i.e., radiolabeled, fluorescent, or hybrid. With image-guided surgery applications in mind, this review discusses these compounds based on clinical need. Here, the focus is on the chemical aspects (e.g., imaging label, spacer moiety, and targeting vector) and their impact on in vitro and in vivo tracer characteristics (e.g., affinity, tumor uptake, and clearance pattern).
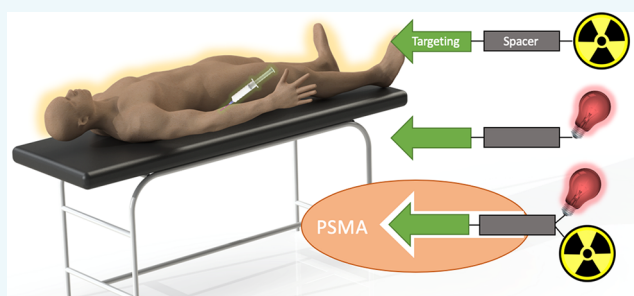
INTRODUCTION

There has been a surge in interest in the diagnosis, staging, and treatment of prostate cancer (PCa), the second most frequent cancer and the fifth leading cause of cancer deaths in men.[1,2] PCa is highly heterogeneous: its manifestation ranges from indolent, slow-growing, low-grade tumors, to high-grade aggressive neoplasms with extensive metastasis that eventually are the cause of mortality.[3] Overexpression of PSMA in >90% of PCa patients[2,4] has driven the development of PSMA-targeted tracers for imaging purposes. PSMA-targeted tracers come in all shapes and sizes (including proteins and nanoparticles), yet the clinical standard is set by glutamate−ureido-based "small-molecule" imaging agents designed to facilitate positron emission tomography (PET) imaging (e.g., **68Ga-PSMA-11**, **68Ga-PSMA-617**, **18F-DCFPyL**, and **18F-PSMA-1007**).[5] PSMA-targeted tracers provide sensitive detection of metastatic lesions both at low PSA values[6−10] and at tumor diameters <5 mm,[11] and have been successfully used to deliver PSMA-targeted endoradiotherapy[12] and theranostics[13] in heavily metastasized castration-resistant PCa patients.

Surgery remains the mainstay of primary PCa treatment;[14] surgery is used for (1) resection of the primary cancer (prostatectomy) and (2) management of locoregional progressive disease in PCa management.[15] For surgery, pre- and perioperative imaging of lymph nodal tumor infiltration and extracapsular tumor expansion (ECE) remain a challenge to date.[16,17] At the moment, image-guidance targets in prostate cancer surgery are confined to sentinel- and/or PSMA-overexpressing lymph nodes.[18] To realize precision PSMA-targeted PCa surgery, preoperative molecular imaging "roadmaps" supplied by PSMA−PET need to be transferred to the surgical setting, indicating a demand for interventional PSMA-targeted imaging techniques.[19,20] Molecular image-guided surgery can be divided into three classes, i.e., tracers for (1) radioguided surgery (positron emission tomography, PET; single-photon emission computed tomography, SPECT; and Cerenkov), (2) fluorescence-guided surgery, and (3) bimodal, i.e., hybrid approaches (SPECT/fluorescence or PET/fluorescence combinations). When these concepts are applied to small-molecule PSMA-targeted tracers, each class requires a different chemical design. Nonetheless, in all three cases tracer designs for image-guided surgery purposes should complement
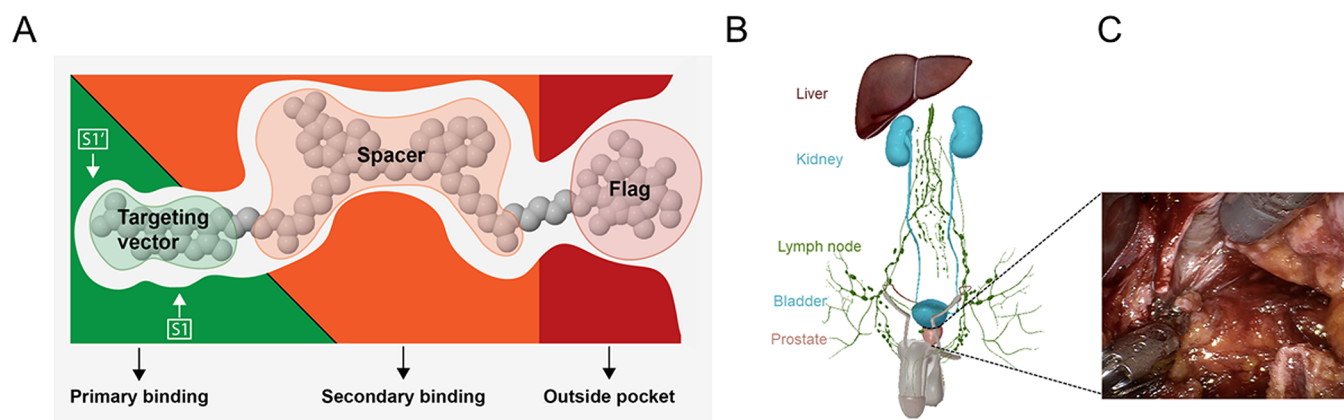
Figure 1. (A) Schematic cross-section view of PSMA illustrating intrinsic interactions between the three critical tracer components (targeting vector, spacer, and imaging flag) and the protein's primary and secondary binding site. (B) Depiction of anatomical relevance in PCa surgery: bladder (in blue) relative to liver (red), kidneys (blue), lymph nodes (green), and prostate (pink). (C) Typical intraoperative sight during radical prostatectomy using nerve-sparing surgery.

existing diagnostic imaging strategies that make use of the clinically accepted glutamate−ureido-based radiotracers for PSMA−PET.

A plethora of PSMA-targeted tracer designs has been presented with image-guided surgery applications in mind, including tracers that already are available for image-guided surgery in the clinic. In this review, we aim at complementing earlier reviews on PSMA-guided surgery[20−23] by discussing: (1) the compatibility of glutamate−ureido-based "small-molecule" PSMA-targeted tracer designs with the binding pocket of PSMA, (2) the influence of tracer design on pharmacokinetics, and (3) the ability of a given design with all its characteristics to address the needs of a surgeon. In doing so, (radio)chemists, nuclear medicine physicians, and surgeons are familiarized with the status quo of small-molecule PSMA-targeted tracers for image-guided surgery.

THE BIOLOGY OF PSMA

PSMA goes by different names, i.e., N-acetyl-L-aspartyl-L-glutamate peptidase I (NAALADase I) in the nervous system and the more generally applicable name glutamate carboxypeptidase II (GCP II). The protein is encoded by folate hydrolase 1 (FOLH1) in humans[24] and has an extracellular domain performing enzymatic functions.[25,26] When PSMA is internalized, it activates the Protein Kinase B (AKT) and mitogen-activated protein kinase pathways, thus promoting proliferation and survival.[27,28]

PSMA is expressed in all human prostate cells, including normal and hyperplastic epithelium and prostatic−intraepithelial neoplasia.[2] In prostate adenocarcinoma, a 100- to 1000-fold overexpression of PSMA is seen compared to benign prostate tissue.[29] The level of PSMA expression correlates with tumor aggressiveness[24] and Gleason score.[30] Next to its expression on prostate cancer, PSMA is also expressed on the endothelial cells of tumor-associated neovasculature of cancers such as lung carcinoma and neuroendocrine carcinoma of the pancreas.[31] This characteristic implies that PSMA-targeting strategies could serve oncological challenges beyond prostate cancer in the future.

PSMA expression levels may be influenced by hormonal therapies commonly applied in prostate cancer. Since androgens downregulate FOLH1 gene expression,[32] short-term androgen deprivation therapy (ADT) enhances PSMA expression.[6] On

the other hand, long-term ADT will decrease tumor volume and thereby limit the potential of PSMA-based imaging.[33]

REQUIREMENTS FOR TARGETING PSMA

The apical domain of the extracellular portion of PSMA provides the target for small-molecule inhibitors as it contains the binuclear-zinc-ion-containing active site of the protein, which can be reached via a 20-Å-deep substrate-binding cavity (Figure 1A).[34,35] PSMA has two substrate-binding pockets within this cavity designated the S1 and S1′ pocket. The S1 pocket is fairly specific for glutamate and aspartate side chains and this pocket is optimized for binding of glutamate and glutamate-like residues.[36] The S1′ pocket is amphipathic, i.e., it exploits both polar (hydrogen-bonding, ionic) and nonpolar (hydrophobic, van der Waals) interactions to induce binding and stabilization of the substrate or inhibitor moieties.[37,38] Low nanomolar PSMA inhibition of this binding site can be achieved through small-molecule moieties of different compositions: phosphonates such as 2-(phosphonomethyl)pentanedioic acid,[39] thiols such as 2-(3-mercaptopropyl) pentanedioic acid,[40] and ureas such as N-[[[(1S)-1-carboxy-3-methylbutyl]amino]carbonyl]-L-glutamic acid.[41] Tracer designs have only been based on organophosphorus-based (mimicking phosphinic acid inhibitors of PSMA) and glutamate−ureido-based (mimicking N-acetylaspartylglutamate) moieties, of which the latter are most abundantly exploited and thus described in this review.

Based on crystallographic data, Barinka et al.[42] have described the existence of a "remote hydrophobic binding register" or rather "accessory hydrophobic pocket" that is formed by portions of β-sheets β13 (Arg463−Asp465) and β14 (Arg534−Arg536). This secondary binding pocket allows for binding of distally placed benzene-like moieties. Exploration of this pocket has led to various structure−activity relationship studies to determine, e.g., optimal spacer length between targeting vector and the benzene-like structure.[43,44] In radiochemistry, exploring the beneficial features of this secondary binding site has proven to be of paramount importance in tracer refinement.[26]

Imaging labels (e.g., radioisotopes, chelates, or fluorophores) are generally placed outside of the amphipathic entrance funnel (Figure 1A). These moieties can impact the affinity; from radiochemical efforts, it seems that mostly steric hindrance and/or charge play a large role in these influences.[13,26,36,43,45−48] For

Scheme 1. Chemical Structures of PSMA-Targeted Tracers for PET and SPECT Imaging[a]
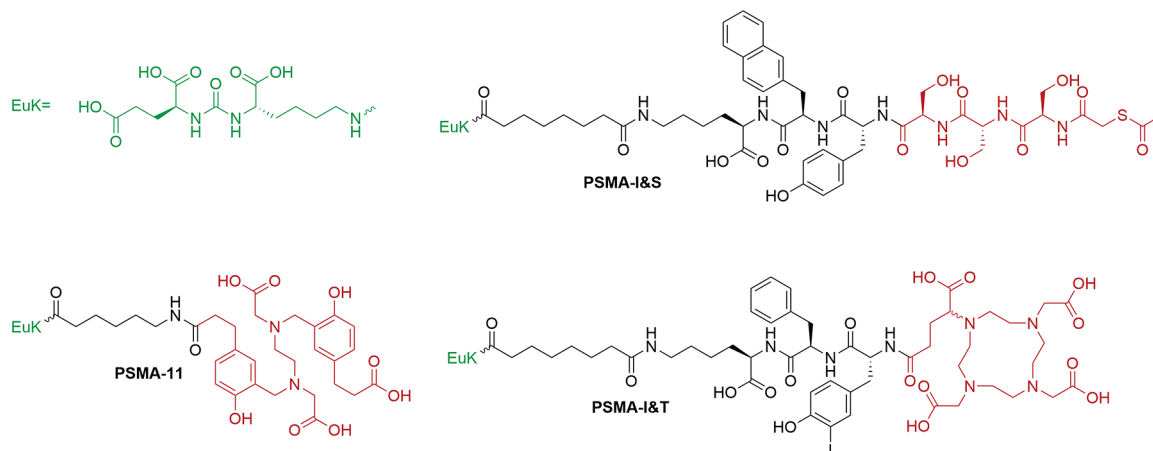
[a]Targeting moiety (green) and imaging flag (red) have been colored accordingly.

example, Banerjee et al.[49] placed various tridentate moieties (chelating ^{99m}Tc) outside the amphipathic entrance funnel, resulting in a more than 60-fold increase in tracer affinity compared to analogs without a spacer moiety.

In an ideal setting, the above-mentioned characteristics imply that small-molecule PSMA-targeted tracers should be designed to meet three requirements: (1) enforcing primary binding with the S1/S1′ pocket(s) and Zn^{2+} ions located in the active site; (2) promoting secondary binding in the accessory hydrophobic pocket; (3) minimizing the impact of the externally placed imaging label (Figure 1A) on the binding affinity with the use of lengthy spacer moieties as previously researched for radio-tracers.[25,36,43,47,49]

SURGICAL REQUIREMENTS

PSMA-targeted image-guided surgery can, in theory, address a number of challenges during PCa surgery. A first surgical application is found in the identification of locoregional metastatic lymph nodes (LN; Figure 1B).[18,50−52] In primary surgery, identifying disease-related LNs by lymphatic mapping has been shown to complement extended pelvic LN dissections.[18,53] The same may be true for PSMA-targeted image guidance approaches. Alternatively, in recurrent PCa, salvage surgery can address the resection of PSMA−PET-positive LNs.[54] However, as is well-known, PET-based detection of PSMA-positive nodes is size-dependent; analyses have shown PSMA−PET detection rates of 0% and >60% when the short axis diameter of the metastatic lesion was ≤2.0 and 2−4.9 mm, respectively.[55,56] This characteristic, combined with the fact that the amount of tracer uptake in micrometastases will lead to an insufficient signal-to-background ratio, implies that PSMA-targeted image-guided surgery is limited to the surgical treatment of macrometastases.[18] Still, patient selection based on the PSMA-based PET scan as well as other clinical variables (PSA value, number of lesions, location of lesions, time from first treatment, Gleason score, and presence of androgen deprivation therapy) remains mandatory.[57]

A second image-guided surgery application is found in defining surgical margins during prostatectomy (Figure 1C). Intraoperative margin assessment is of particular relevance when both ECEs might be present and a nerve-sparing radical prostatectomy is intended (to preserve erectile function). The diagnostic accuracy of current imaging methods in predicting

ECE is poor. Intraoperatively, the ex vivo neurovascular structure-adjacent frozen-section examination (NeuroSAFE) technique can be used to study excised tissue and to pathologically assess the presence of tumor cells in the resection margins.[58,59] Intraoperative assessment of margins would improve surgical logistics and would also improve prediction of the presence of residual lesions in the patient.

Despite the specificity for PCa, basal PSMA expression has also been reported for other tissues, including benign prostate epithelium.[2,60] Basal PSMA expression may thus provide a background signal that needs to be considered when margin assessment is aimed for. While glutamate−ureido-based radio-tracers have readily proven their ability to target the primary tumor,[61] their predominant renal clearance could also compromise margin assessment; during prostatectomy, the bladder is disconnected from the prostate and urine might flow into the surgical field (Figure 1B). If urine contains PSMA-targeted tracer (or its metabolites), it can contaminate the margins and impair the ability to surgically assess the tumor spread relative to the background.[56] However, renal excretion rates are unknown for most tracers. While the renal cortex is said to express PSMA,[2,60,62−66] studies with the PSMA-targeted radiolabeled J591 monoclonal antibody did not confirm its presence.[67,68] As the proximal tubules are the prime location for a plethora of transporters and multiligand receptors such as megalin and cubilin, alternative mechanisms could potentially also influence renal accumulation.[69−71] The observation of ^{177}Lu-PSMA I&T depicting an 8-fold reduction in kidney uptake/retention at late (24−48 h) compared to early (1−4 h) time points strengthens the assumption that metabolism of renally accumulated PSMA-targeted tracers could influence urine contamination.[72] It is thus assumable that renal tracer retention can to a certain degree be predictive for the presence of imaging agents or labels in urine. To avoid such contamination during surgery, a tracer either should not undergo renal clearance or the time between tracer administration and surgery should be extended to minimize contamination.

The physics of intraoperative guidance is dictated to a large degree by two related features, i.e., the tissue penetration of the imaging signature and the intensity of the signal. Identification of affected LNs is likely to demand imaging signatures that can readily penetrate tissue, as metastases are embedded in, e.g., adipose tissue, and can be rather small, hence favoring

radioguidance modalities.[73] The assessment of ECE in the dissection planes requires a superficial feedback as signal from deeper-lying tissues limits the spatial resolution. This requirement may be optimally supported by the use of optical technologies. However, the availability of surgical modalities that enable detection of the tracer used for guidance is imperative. While perhaps not immediately obvious, the surgical technique itself may also influence the choice for a particular tracer. During open surgery, a small (approximately 15×10 cm^2) but deep cavity is created that can easily accommodate a γ-probe but limits the use of a 2D fluorescence camera. In a (robot-assisted) laparoscopic setting, on the other hand, dedicated (DROP-IN) γ-probes are required for radiotracing, while the availability of a fluorescence (and 3D) laparoscopic system is quickly becoming standard practice.[74] For example, since the Da Vinci S model has become available, all these surgical robots are equipped with a fluorescence camera capable of imaging different fluorophores.[74,75]

The preceding paragraph implies that PSMA-targeted image-guided surgery is limited to the surgical treatment of macrometastases and defining the surgical margins. Both applications require a high signal-to-background ratio and benefit from minimal tracer presence in urine.

PSMA-TARGETED TRACERS

Tracers for PSMA-Targeted Radioguided Surgery. The field of radioguided surgery revolves around the intraoperative use of oftentimes diagnostic radiotracers commonly used in the field of nuclear medicine. In this concept, noninvasive preoperative images can be used to provide both a surgical roadmap and intraoperative guidance. A range of radioactive isotopes, corresponding chelates, and combinations thereof have been coupled to PSMA-targeted vectors, thereby developing a variety of radiotracers. Unique for PSMA-targeted radiotracers is that many of them have already been translated to the clinic. Interestingly, relatively few preclinical efforts with image-guided surgery in mind have been reported in this area. (Scheme 1, Table 1, Figure 2).

Use of Established PSMA–PET Tracers for Image-Guidance Purposes. During patient selection for PSMA-targeted image-guided surgery, the availability of, e.g., diagnostic PSMA–PET images, has proven to be a critical prerequisite (Figure 2A).[77] Intraoperatively, radiotracers such as ^{68}Ga-PSMA-11[78] can potentially be traced via their β^+-emission ($E_{max}\beta^+ = 1899$ keV), high-energy γ-emission ($E\gamma = 511$ keV), or Cerenkov light (>250 nm). Despite literature examples regarding intraoperative high-energy γ-emission tracing of PET tracers,[79] this application has not yet been reported for PSMA. Tracing the β^+-emission of ^{68}Ga-PSMA-11 ($IC_{50} = 7.5 \pm 2.2$)[78] is currently being investigated for ex vivo margin assessment in primary PCa and to identify PSMA-positive LNs,[80] even though this emission type is limited by its tissue penetration of a few millimeters.[81] Alternatively, Costa et al.[82] have used ex vivo Cerenkov imaging to identify ^{68}Ga-PSMA-11 uptake in prostate sections containing primary PCa lesions. Despite the potential displayed by these technologies, the half-life of ^{68}Ga ($t_{1/2, rad} = 1.1$ h) limits the surgical time frame, the radiation dose to the surgical staff is potentially high,[83,84] and renal clearance of ^{68}Ga-PSMA-11 (kidney retention 139.4 ± 21.4%ID/g at 1 h) means that prostate samples need to be rinsed prior to imaging to remove urine contamination. Furthermore, the signal penetration of β^+-emissions (mm range)[81] and the resulting Cerenkov luminescence (<2 mm)[85] limits the

Table 1. Radioisotope-Based PSMA-Targeted Tracers for Image-Guided Surgery

compound	receptor affinity (competitor)	tumor-to-background (time point, cell line, background tissue)	kidney-to-tumor (time point, cell line)	injected dose	biodistribution; time point	clearance pathway (time point, uptake clearance organs)	half-life	lipophilicity	plasma protein binding	optimized for entrance funnel?	imaging label	imaging signature (s)
^{68}Ga-PSMA-11[78]	$IC_{50} = 7.5 \pm 2.2$ (2-PMPA)	8^b (1 h, LNCaP, muscle)	18.1 (1 h, LNCaP)	0.1–0.2 (10–20 MBq/nmol)	Yes; 1 h	Renal (1 h, kidneys 139.4 ± 21.4%ID/g, liver 0.87 ± 0.05% ID/g)	$t_{1/2, rad} = 1.1$ h	LogP = −3.15^a	Data not provided	Yes	HBED-CC, ^{68}Ga	β ($E_{max}\beta^+$ = 1899 keV), γ ($E\gamma$ = 511 keV), Cerenkov (>250 nm)
^{111}In-PSMA I&T[48]	$IC_{50} = 7.5 \pm 1.5$ nM ((^{125}I-BA)KuE)	43 ± 6 (1 h, LNCaP, muscle)	23.8 (1 h, LNCaP)	0.2 nmol (7 MBq/nmol)	Yes; 1 h	Renal (1 h, kidneys, 191 ± 24%ID/g, liver 0.26 ± 0.04%ID/g)	$t_{1/2, rad} = 67$ h	LogP = −4.5	83%[93]	Yes	DOTAGA, ^{111}In	γ ($E\gamma$ = 171.3, 245.4 keV)
^{99m}Tc-PSMA I&S[93]	$IC_{50} = 39.7 \pm 1.2$ nM((^{125}I-BA)KuE)	21 (1 h, LNCaP, muscle)	22.5 (1 h, LNCaP)	0.1 nmol (30–40 MBq/nmol)	Yes; 1 h, 3 h, 5 h, 12 h, 16 h, 21 h	Renal (1 h, kidneys 186 ± 23%ID/g, liver 1.58 ± 0.24%ID/g)	$t_{1/2, rad} = 6.5$ h	LogP = −3.0	94%	Yes	mas$_3$, ^{99m}Tc	γ ($E\gamma$ = 140.5 keV)

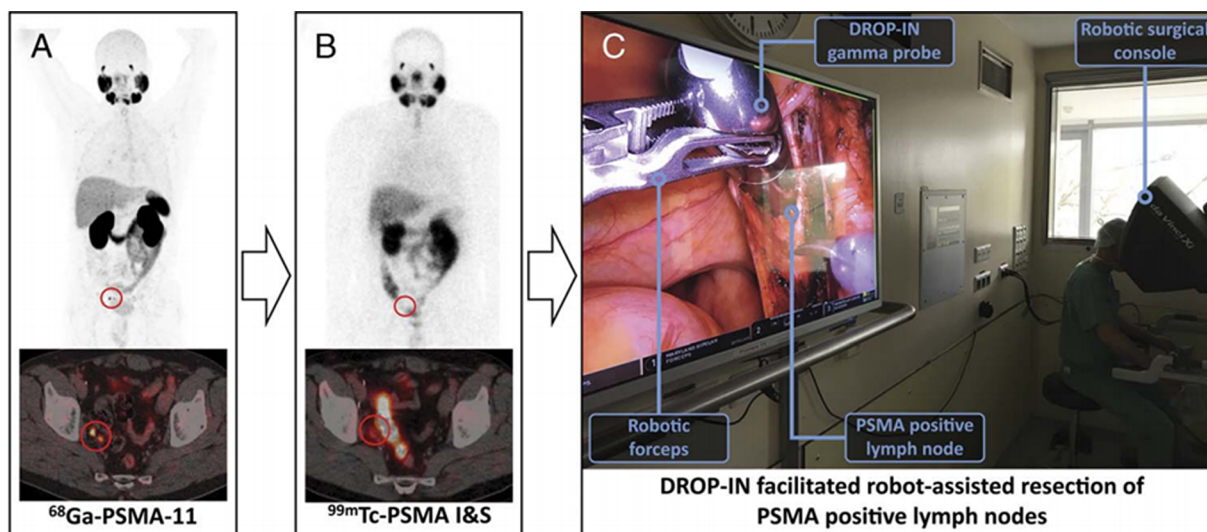^{a}Values were calculated by using ChemAxon's Chemicalize plugin. ^{b}Estimated from graph.

Figure 2. Typical clinical workflow of radioguided surgery: (A) preoperative ^{68}Ga-PSMA-11 PET/CT followed by (B) preoperative ^{99m}Tc-PSMA I&S SPECT/CT; (C) intraoperative guidance combined with minimally invasive robot-assisted laparoscopic surgery using a DROP-IN γ-probe with ^{99m}Tc-PSMA I&S. (Reprinted from van Leeuwen et al.[76] with permission from Wolters Kluwer Health, Inc.).

implementation to superficial lesions. On a positive note, these technologies are also applicable for alternative PET tracers such as, e.g., ^{18}F-PSMA-1007 (minimized renal clearance and extended half-life).[86] With regard to half-life, the use of, e.g., ^{64}Cu-based derivatives ($t_{1/2}$ = 12.7 h, $E_{max}\beta^+$ = 653 keV)[87] could potentially help to further extend the time interval between tracer administration and surgery.

SPECT Tracers for PSMA-Targeted Image-Guided Surgery. In the field of radioguided surgery, γ-ray-emitting radiotracers are most commonly implemented.[83] Herein, radionuclides such as [125]I ($E\gamma$ = 31.0, 35.5, 27.2, 27.4 keV), [177]Lu (113, 210 keV), [99m]Tc ($E\gamma$ = 140.5 keV), and [111]In ($E\gamma$ = 171.3, 245.4 keV) have proven to be compatible with conventional γ-probes.[81] Given the clinical use of the chemically optimized ^{68}Ga-PSMA I&T, wherein a peptidic 3-iodo-D-Tyr-D-Phe spacer promotes secondary binding,[13] and the ability of the 1,4,7,10-tetraazacyclododecane-1,4,7,10-tetraacetic acid (DO-TAGA) chelate to coordinate ^{111}In, ^{111}In-PSMA I&T was explored in radioguided surgery applications.[88,89] In direct comparison, the [nat]In-PSMA I&T (7.5 ± 1.5 nM)[48] showed a similar affinity for PSMA compared to its [nat]Ga and [nat]Lu-labeled analogs (9.4 ± 2.9 and 7.9 ± 2.4 nM, respectively). Clinical evaluation of ^{111}In-PSMA I&T in six patients revealed that although the sensitivity and spatial resolution of ^{111}In SPECT/CT are limited, uptake of the tracer in PSMA-positive LNs could be used to provide efficient surgical guidance.[77,88] Theoretically, tracer analogs like ^{111}In-PSMA-617[90] could also be explored in a similar radioguided surgery setting. To circumvent the suboptimal nuclear properties of [111]In (high cost, limited availability of [111]InCl₃, relatively poor SPECT quality, and high burden of radiation), a demand for a tracer analog labeled with ^{99m}Tc arose, ^{99m}Tc is one of the—if not *the*—most important radionuclide(s) used in nuclear medicine due to its availability from a generator, convenient half-life, negligible radiation dose to the patient, and low cost.[83] Given the versatile but very specific coordination chemistry of ^{99m}Tc,[91] various ^{99m}Tc-chelating moieties used in PSMA-targeted radiotracers have been described.[47,49,62,92−95] [99m]Tc PSMA I&S (IC$_{50}$ = 39.7 ± 1.2 nM)[93] employs the mas₃ chelate, and to optimize interaction with the accessory hydrophobic pocket in the PSMA protein the

tracer contains a D-Tyr-D-2-Nal-D-Lys spacer moiety. The lipophilicity of **PSMA I&S** (LogP = −3.0) is higher compared to its parent analog **PSMA-I&T** (LogP = −4.5), resulting in delayed blood clearance (^{99m}Tc PSMA I&S 1.73 ± 0.50%ID/g; ^{111}In PSMA I&T 0.24 ± 0.05%ID/g). [99m]Tc PSMA I&S provides high-contrast preoperative PSMA-SPECT (at time points >4 h post injection, preferably 18 h) and supports tracing with a traditional γ-probe in open surgery,[93,96] or during robot-assisted surgery with a DROP-IN γ-probe (Figure 2B,C).[76] To date, this tracer has predominantly been used in patients that have received salvage surgery of metastasized LNs.[57,96] Following PSMA-guided surgery, a complete biochemical response (PSA < 0.2 ng/mL) could be achieved in 66% of 121 patients.[57] Notably, the clinical studies did also indicate that PSMA-guided surgery was particularly valuable in patients with low preoperative PSA values that displayed a single lesion on PSMA−PET.

The radioguided surgery studies have relied heavily on previous research and expertise obtained in the field of radiochemistry. Efforts are focused on both primary PCa as well as nodal metastases and set the current standard for PSMA-targeted image-guided surgery applications.

PSMA-Targeted Fluorescent Tracers. In contrast to tracers for radioguided surgery, fluorescent PSMA-targeted tracers have the potential to support real-time optical visualization of PSMA-positive lesions. Unfortunately, the ability to use this technique for lesion identification is limited to superficial applications (<1 cm from the surface), meaning it cannot be used to create surgical roadmaps.[97] Preclinically, various fluorescent PSMA-targeted tracers have been described; designs greatly vary in spacer moieties and fluorophores (visible to far-red fluorophores and near-infrared fluorophores). (Tables 2, 3, Schemes 2, 3, and Figure 3.)

Visible to Far-Red Fluorescent PSMA-Targeted Tracers. Since evaluation conditions varied in, e.g., dose and time points, insights can only be inferred from direct comparisons that have been made in individual studies. For the same reason, it is difficult to discuss the findings of studies that reported individual compounds, i.e., **CYUE-Rhodamine B**,[98] **PSMA-1-Cy5.5**,[99] and **YC-9**.[100]

Table 2. Visible to Far-Red Fluorescent Imaging Agents for PSMA-Targeted Fluorescence-Guided Surgery

compound	receptor affinity (competitor)	tumor uptake (time point, cell line)	kidney uptake (time point, cell line)	injected dose	biodistribution; time point	clearance pathway (time point, uptake clearance organs)	half-life	lipophilicity	plasma protein binding	optimized for entrance funnel?	imaging label	imaging signature(s)
CYUE-Rhodamine B[98]	k_D = 88 nM (2-PMPA)	No ex vivo quantification, no scale bars	No ex vivo quantification, no scale bars	No in/ex vivo experiments performed	No in/ex vivo experiments performed	No in/ex vivo experiments performed	No in/ex vivo experiments performed	LogP = −0.37[a]	Data not provided	Yes	Rhodamine-B (427 g/mol)	λ_{abs} = 510 nm, λ_{em} = 565 nm
DUPA-Dylight 680[46]	k_D = 33 nM (2-PMPA)	No ex vivo quantification, no scale bars	No ex vivo quantification, no scale bars	10 nmol	No ex vivo quantification, no scale bars	No ex vivo quantification, no scale bars	Data not provided	LogP = 1.38[a]	Data not provided	Yes	DyLight 680 (790 g/mol)	λ_{abs} = 682 nm, λ_{em} = 715 nm
DUPA-Alexa Fluor 647[46]	k_D = 4.5 nM (2-PMPA)	No ex vivo quantification, no scale bars	No ex vivo quantification, no scale bars	10 nmol	No ex vivo quantification, no scale bars	No ex vivo quantification, no scale bars	Data not provided	Fluorophore structure not available	Data not provided	Yes	AlexaFluor 647 (853 g/mol)	λ_{abs} = 650 nm, λ_{em} = 670 nm
PSMA-1-Cy5.5[99]	IC_{50} = 2.1 ± 0.1 nM (Glutamate-ureido-cysteine)	5.08%ID (24 h, PC3-PIP) 2, 3, 7, 17, 18, 16, 51, 51, 50, 43, 41, 41 AU[b] (at 0.8, 0.17, 0.5, 1, 2, 6, 8, 24, 48, 72, 96, and 120 h PC3-PIP (in vivo))	0.025 AU[c] (120 h, PC3-PIP)	1 nmol	Qualitative; 0.8, 0.17, 0.5, 1, 2, 4, 6, 8, 24, 48, 72, 96, and 120 h (in vivo); Qualitative; 120 h (ex vivo)	Renal (120 h, kidneys 0.025 AU[c], liver 0.01 AU[c])	Data not provided	LogP = −1.02 ± 0.23	Data not provided	Yes	Cy5.5 (567 g/mol)	λ_{abs} = 675 nm, λ_{em} = 694 nm
Cy5.5-1[101]	k_i = 90 ± 40 pM (NAAG)	30000 AU[c] (24 h, PC3-PIP)	60000 AU[c] (24 h, PC3-PIP)	1 nmol	Qualitative; 1, 4, 24 h	Renal (24 h, kidneys 60000 AU[c], liver 10000 AU[c])	Data not provided	LogP = 0.12[a]	Data not provided	Yes	Tetrakis sulfonate Cy5.5 (897 g/mol)	λ_{abs} = 675 nm, λ_{em} = 694 nm
Cy5.5-2[101]	k_i = 50 ± 20 pM (NAAG)	50000 AU[c] (24 h, PC3-PIP)	50000 AU[c] (24 h, PC3-PIP)	1 nmol	Qualitative; 1, 4, 24 h	Renal (24 h, kidneys 50000 AU[c], liver 10000 AU[c])	Data not provided	LogP = −1.08[a]	Data not provided	Yes	Tetrakis sulfonate Cy5.5 (897 g/mol)	λ_{abs} = 675 nm, λ_{em} = 694 nm
Cy5.5-3[101]	k_i = 50 ± 2 pM (NAAG)	70000 AU[c] (24 h, PC3-PIP)	50000 AU[c] (24 h, PC3-PIP)	1 nmol	Qualitative; 1, 4, 24 h	Renal (24 h, kidneys 50000 AU[c], liver 10000 AU[c])	Data not provided	LogP = 3.00[a]	Data not provided	Yes	Tetrakis sulfonate Cy5.5 (897 g/mol)	λ_{abs} = 675 nm, λ_{em} = 694 nm
Cy5.5(SO3−)4-EuK[102]	k_i = 0.6 ± 0.1 nM (NAAG)	3700 AU[b] (24 h, 22Rv1)	24000 AU[c] (24 h, 22Rv1)	10 nmol	Qualitative; 1, 2, 4, 24 h	Renal (24 h, kidneys 24000 AU[c], liver 3540 AU[c])	Data not provided	LogP = −1.36[a]	Data not provided	No	Tetrakis sulfonate Cy5.5 (897 g/mol)	λ_{abs} = 675 nm, λ_{em} = 694 nm
Cy5.5(SO3−)4-(EuK)2[102]	k_i = 0.1 ± 0.0 nM (NAAG)	5000 AU[b] (24 h, 22Rv1)	20000 AU[c] (24 h, 22Rv1)	10 nmol	Qualitative; 1, 2, 4, 24 h	Renal (24 h, kidneys 20000 AU[c], liver 0 AU[c])	Data not provided.	LogP = −0.33[a]	Data not provided	No	Tetrakis sulfonate Cy5.5 (897 g/mol)	λ_{abs} = 675 nm, λ_{em} = 694 nm
Cy5.5(SO3−)4(aminomethyl)benzoic acid-(EuK)2[102]	k_i = 0.4 ± 0.1 nM (NAAG)	5300 AU[b] (24 h, 22Rv1)	20000 AU[c] (24 h, 22Rv1)	10 nmol	Qualitative; 1, 2, 4, 24 h	Renal (24 h, kidneys 20000 AU[c], liver 3540 AU[c])	Data not provided	LogP = 1.32[a]k	Data not provided	No	Tetrakis sulfonate Cy5.5 (897 g/mol)	λ_{abs} = 675 nm, λ_{em} = 694 nm
Cy5.5(SO3−)4-2-nitroimidazole-EuK[103]	k_i = 0.3 ± 0.0 nM (NAAG)	18 AU[b] (24 h, 22Rv1)	29 AU[b] (24 h, 22Rv1)	10 nmol	Qualitative; 1, 2, 4, 24 h	Renal (24 h, kidneys 29 AU[b], liver 15 AU[b])	Data not provided	LogP = −0.31[a]	Data not provided	No	Tetrakis sulfonate Cy5.5 (897 g/mol)	λ_{abs} = 675 nm, λ_{em} = 694 nm
Cy5.5(SO3−)4(2-nitroimidazole)2-EuK[103]	k_i = 3.0 ± 0.3 nM (NAAG)	20 AU[b] (24 h, 22Rv1)	46 AU[b] (24 h, 22Rv1)	10 nmol	Qualitative; 1, 2, 4, 24 h	Renal (24 h, kidneys 46 AU[b], liver 13 AU[b])	Data not provided	LogP = −2.24[a]	Data not provided	No	Tetrakis sulfonate Cy5.5 (897 g/mol)	λ_{abs} = 675 nm, λ_{em} = 694 nm
YC-9[100]	k_i = 0.2 ± 0.05 nM (NAAG)	15 AU[c] (24 h, PC3-PIP)	25 AU[c] (24 h, PC3-PIP)	10 nmol	Qualitative; 6 h	Renal (24 h, kidneys 25 AU[c], liver 3 AU[c])	Data not provided	LogP = −12.72[a]	Data not provided	Yes	IRDye700DX (1635 g/mol)	λ_{abs} = 689 nm, λ_{em} = 700 nm

[a]Values were calculated by using ChemAxon's Chemicalize plugin. [b]Estimated from graph. [c]Estimated from scale bar. AU = arbitrary units.

Table 3. Near-Infrared Imaging Agents for PSMA-Targeted Fluorescence-Guided Surgery

| compound	receptor affinity (competitor)	tumor uptake (time point, cell line)	kidney uptake (time point, cell line)	injected dose	biodistribution; time point	clearance pathway (time point, uptake clearance organs)	half-life	lipophilicity	plasma protein binding	optimized for entrance funnel?	imaging label	imaging signature(s)
Cy7–1[101]	$k_i = 1.0 \pm 0.5$ pM (NAAG)	30 AU^{db} (24 h, PC3-PIP)	20 AU^{db} (24 h, PC3-PIP)	1 nmol	Quantitative, 24 h	Renal (24 h, kidneys 20 AU^{db}, liver 10 AU^{db})	Data not provided	LogP = 3.39^a	Data not provided	Yes	Cy7 (665 g/mol)	$\lambda_{abs} = 753$ nm, $\lambda_{em} = 775$ nm
Cy7–2[101]	$k_i = 7.0 \pm 0.4$ pM (NAAG)	200 AU^{db} (24 h, PC3-PIP)	28 AU^{db} (24 h, PC3-PIP)	1 nmol	Quantitative; 24 h	Renal (24 h, kidneys 28 AU^{db}, liver 10 AU^{db})	Data not provided	LogP = 2.19^a	Data not provided	Yes	Cy7 (665 g/mol)	$\lambda_{abs} = 753$ nm, $\lambda_{em} = 775$ nm
Cy7–3[101]	$k_i = 5.0 \pm 0.2$ pM (NAAG)	200 AU^{db} (24 h, PC3-PIP)	30 AU^{db} (24 h, PC3-PIP)	1 nmol	Quantitative; 24 h	Renal (24 h, kidneys 30 AU^{db}, liver 10 AU^{db})	Data not provided	LogP = 3.18^a	Data not provided	Yes	Cy7 (665 g/mol)	$\lambda_{abs} = 753$ nm, $\lambda_{em} = 775$ nm
IRDye800CW-1[101]	$k_i = 70 \pm 5$ pM (NAAG)	500 AU^{db} (24 h, PC3-PIP)	3000 AU^{db} (24 h, PC3-PIP)	1 nmol	Quantitative; 1, 2, 4, 24 h	Renal (24 h, kidneys 3000 AU^{db}, liver 28 AU^{db})	Data not provided	LogP = 2.45^a	Data not provided	Yes	IRDye800CW (983 g/mol)	$\lambda_{abs} = 774$ nm, $\lambda_{em} = 789$ nm
IRDye800CW-2[101]	$k_i = 40 \pm 10$ pM (NAAG)	2200 AU^{db} (24 h, PC3-PIP)	4000 AU^{db} (24 h, PC3-PIP)	1 nmol	Quantitative; 1, 2, 4, 24 h	Renal (24 h, kidneys 4000 AU^{db}, liver 13 AU^{db})	Data not provided	LogP = 1.25^a	Data not provided	Yes	IRDye800CW (983 g/mol)	$\lambda_{abs} = 774$ nm, $\lambda_{em} = 789$ nm
IRDye800CW-3[101]	$k_i = 20 \pm 5$ pM (NAAG)	3200 AU^{db} (24 h, PC3-PIP)	1100 AU^{db} (24 h, PC3-PIP)	1 nmol	Quantitative; 1, 2, 4, 24 h	Renal (24 h, kidneys 1100 AU^{db}, liver 20 AU^{db})	Data not provided	LogP = 3.21^a	Data not provided	Yes	IRDye800CW (983 g/mol)	$\lambda_{abs} = 774$ nm, $\lambda_{em} = 789$ nm
IRDye800RS-1[101]	$k_i = 100 \pm 10$ pM (NAAG)	0.05 AU^c (24 h, PC3-PIP)	0.10 AU^c (24 h, PC3-PIP)	1 nmol	Qualitative; 1, 2, 4, 24 h	Renal (24 h, kidneys 0.10 AU^c, liver 0.03 AU^c)	Data not provided	LogP = 5.01^a	Data not provided	Yes	IRDye800RS (825 g/mol)	$\lambda_{abs} = 774$ nm, $\lambda_{em} = 789$ nm
IRDye800RS-2[101]	$k_i = 200 \pm 50$ pM (NAAG)	0.20 AU^c (24 h, PC3-PIP)	0.25 AU^c (24 h, PC3-PIP)	1 nmol	Qualitative; 1, 2, 4, 24 h	Renal (24 h, kidneys 0.25 AU^c, liver 0.03 AU^c)	Data not provided	LogP = 3.81^a	Data not provided	Yes	IRDye800RS (825 g/mol)	$\lambda_{abs} = 774$ nm, $\lambda_{em} = 789$ nm
IRDye800RS-3[101]	$k_i = 4 \pm 0.5$ pM (NAAG)	0.29 AU^c (24 h, PC3-PIP)	0.29 AU^c (24 h, PC3-PIP)	1 nmol	Qualitative; 1, 2, 4, 24 h	Renal (24 h, kidneys 0.29 AU^c, liver 0.01 AU^c)	Data not provided	LogP = 5.76^a	Data not provided	Yes	IRDye800RS (825 g/mol)	$\lambda_{abs} = 774$ nm, $\lambda_{em} = 789$ nm
ICG-1[101]	$k_i = 700 \pm 10$ pM (NAAG)	0.05 AU^c (24 h, PC3-PIP)	0.05 AU^c (24 h, PC3-PIP)	1 nmol	Qualitative; 1, 2, 4, 24 h	Renal (24 h, kidneys 0.05 AU^c, liver 0.03 AU^c)	Data not provided	LogP = 5.65^a	Data not provided	Yes	ICG (714 g/mol)	$\lambda_{abs} = 780$ nm, $\lambda_{em} = 800$ nm
ICG-2[101]	$k_i = 400 \pm 60$ pM (NAAG)	0.08 AU^c (24 h, PC3-PIP)	0.10 AU^c (24 h, PC3-PIP)	1 nmol	Qualitative; 1, 2, 4, 24 h	Renal (24 h, kidneys 0.10 AU^c, liver 0.05 AU^c)	Data not provided	LogP = 4.45^a	Data not provided	Yes	ICG (714 g/mol)	$\lambda_{abs} = 780$ nm, $\lambda_{em} = 800$ nm
ICG-3[101]	$k_i = 200 \pm 5$ pM (NAAG)	0.29 AU^c (24 h, PC3-PIP)	0.22 AU^c (24 h, PC3-PIP)	1 nmol	Qualitative; 1, 2, 4, 24 h	Renal (24 h, kidneys 0.22 AU^c, liver 0.05 AU^c)	Data not provided	LogP = 6.40^a	Data not provided	Yes	ICG (714 g/mol)	$\lambda_{abs} = 780$ nm, $\lambda_{em} = 800$ nm
DUPA-IR-Dye800CW[46]	$k_D = 12$ nM (2-PMPA)	No ex vivo quantification, no scale bars	No ex vivo quantification, no scale bars	10 nmol	No ex vivo quantification, no scale bars	No ex vivo quantification, no scale bars	Data not provided	LogP = 0.62^a	Data not provided	Yes	IRDye800CW (983 g/mol)	$\lambda_{abs} = 774$ nm, $\lambda_{em} = 789$ nm

Table 3. continued

compound	receptor affinity (competitor)	tumor uptake (time point, cell line)	kidney uptake (time point, cell line)	injected dose	biodistribution; time point	clearance pathway (time point, uptake clearance organs)	half-life	lipophilicity	plasma protein binding	optimized for entrance funnel?	imaging label	imaging signature(s)
ZJ-MCC-dEdE-dEGK (IRDye800CW)G[106]	Data not provided	No ex vivo quantification, no scale bars	No ex vivo quantification, no scale bars	2–10 nmol	Qualitative; 1, 2, 3, 4 h	No ex vivo quantification, no scale bars	Data not provided	LogP = −2.67[a]	Data not provided	Yes	IRDye800CW (983 g/mol)	λ_{abs} = 774 nm, λ_{em} = 789 nm
PSMA-1-IRDye800[99]	IC$_{50}$ = 1.5 ± 0.1 nM (EuC)	7.12%ID (120 h, PC3-PIP) 28, 35, 52, 58, 71, 65, 60,50, 38, 31, 35, 22 (at 0.8, 0.17, 0.5, 1, 2, 6, 8, 24, 48, 72, 96, and 120 h (in vivo)	0.004 AU[c] (120 h, PC3-PIP)	1 nmol	Qualitative; 0.8, 0.17, 0.5, 1, 2, 6, 8, 24, 48, 72, 96, and 120 h (in vivo), Qualitative; 4 h (ex vivo)	Renal (120 h, kidneys 0.004 AU[c], liver 0.002 AU[c])	Data not provided	LogP = −2.14 ± 0.17	Data not provided	Yes	IRDye800CW (983 g/mol)	λ_{abs} = 774 nm, λ_{em} = 789 nm
EUKL-cRGDfK-IRDye800[107]	Data not provided	1.53 AU[c] (24 h, PC3-PIP)	1.53 AU[c] (24 h, PC3-PIP)	1 nmol	Qualitative; 24 h	Renal (24 h, kidneys 1.53 AU[c], liver 0.5 AU[c])	Data not provided	LogP = −2.21[a]	Data not provided	No	IRDye800CW (983 g/mol)	λ_{abs} = 774 nm, λ_{em} = 789 nm
IRDye800CW-SCE[104]	Data not provided	160 AU[b], 140 AU[b] (12 h, 24 h, LNCaP)	No ex vivo quantification, no scale bars	10 nmol	Qualitative; 12 h, 24 h	No ex vivo quantification, no scale bars	Data not provided	LogP = 0.94[a]	Data not provided	No	IRDye800CW (983 g/mol)	λ_{abs} = 774 nm, λ_{em} = 789 nm
KUE-PEG$_4$-ZW800 + 3C[105]	Data not provided	4 AU[b] (4 h, LNCaP)	13 AU[b] (4 h, LNCaP)	10 nmol	Quantitative; 4 h	Renal (4 h, kidneys 13 AU[b], liver 2.4 AU[b])	$t_{1/2, \text{biol}}$ = 4.8 h	LogP = 1.39[a]	Data not provided	Yes	ZW800−1 (997 g/mol)	λ_{abs} = 772 nm, λ_{em} = 788 nm
OTL78[108]	k_D = 4.7 nM (EuK-FITC)	7.5 AU[c], 15 AU[c], 17.5 AU[c], 11 AU[c], 15 AU[c], 15 AU[c] (2 h, 22Rv1 for 1, 3, 10, 30, 60, 90 nmol)	1.3 AU[c], 1.8 AU[c], 4.1 AU[c], 5.9 AU[c], 4.2 AU[c], 1.0 AU[c] (2 h, 22Rv1 for 1, 3, 10, 30, 60, 90 nmol)	1, 3, 10, 30, 60, 90 nmol	Qualitative; 2 h	Renal (2 h, kidneys 4.1 AU[c], liver 0 AU[c], for 10 nmol)	Data not provided	LogP = 1.19[a]	Data not provided	Yes	S0456 (983 g/mol)	λ_{abs} = 774 nm, λ_{em} = 789 nm

[a]Values were calculated by using ChemAxon's Chemicalize plugin. [b]Estimated from graph. [c]Estimated from scale bar. [d]Normalized to muscle tissue. AU = arbitrary units.

Scheme 2. Chemical Structures of Visible to Far-Red Fluorescent Imaging Agents for PSMA-Targeted Fluorescence-Guided Surgery[a]
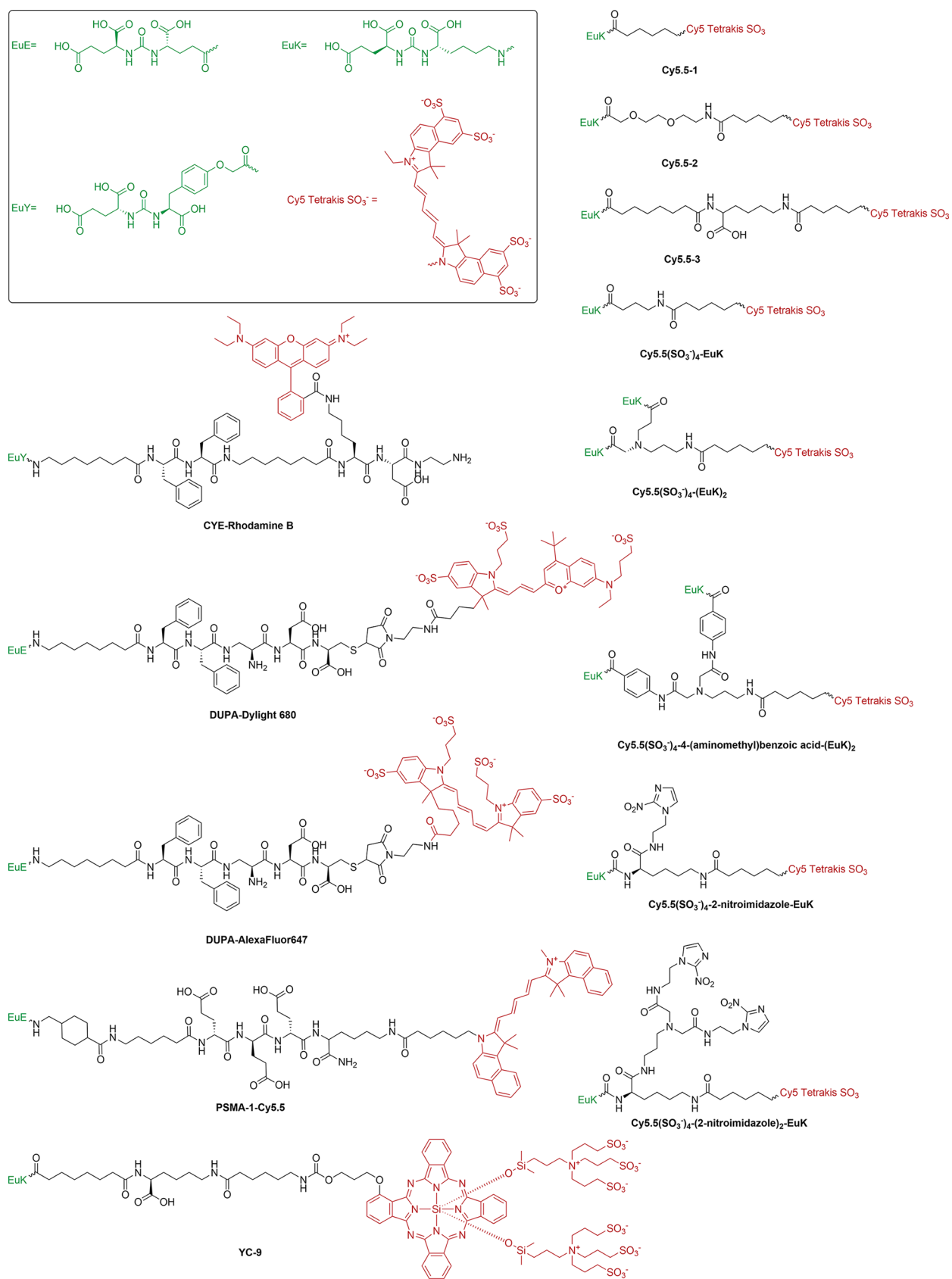
[a]Targeting vector (green) and imaging label (red) were colored accordingly.

Scheme 3. Chemical Structures of Near-Infrared Imaging Agents for PSMA-Targeted Fluorescence-Guided Surgery[a]
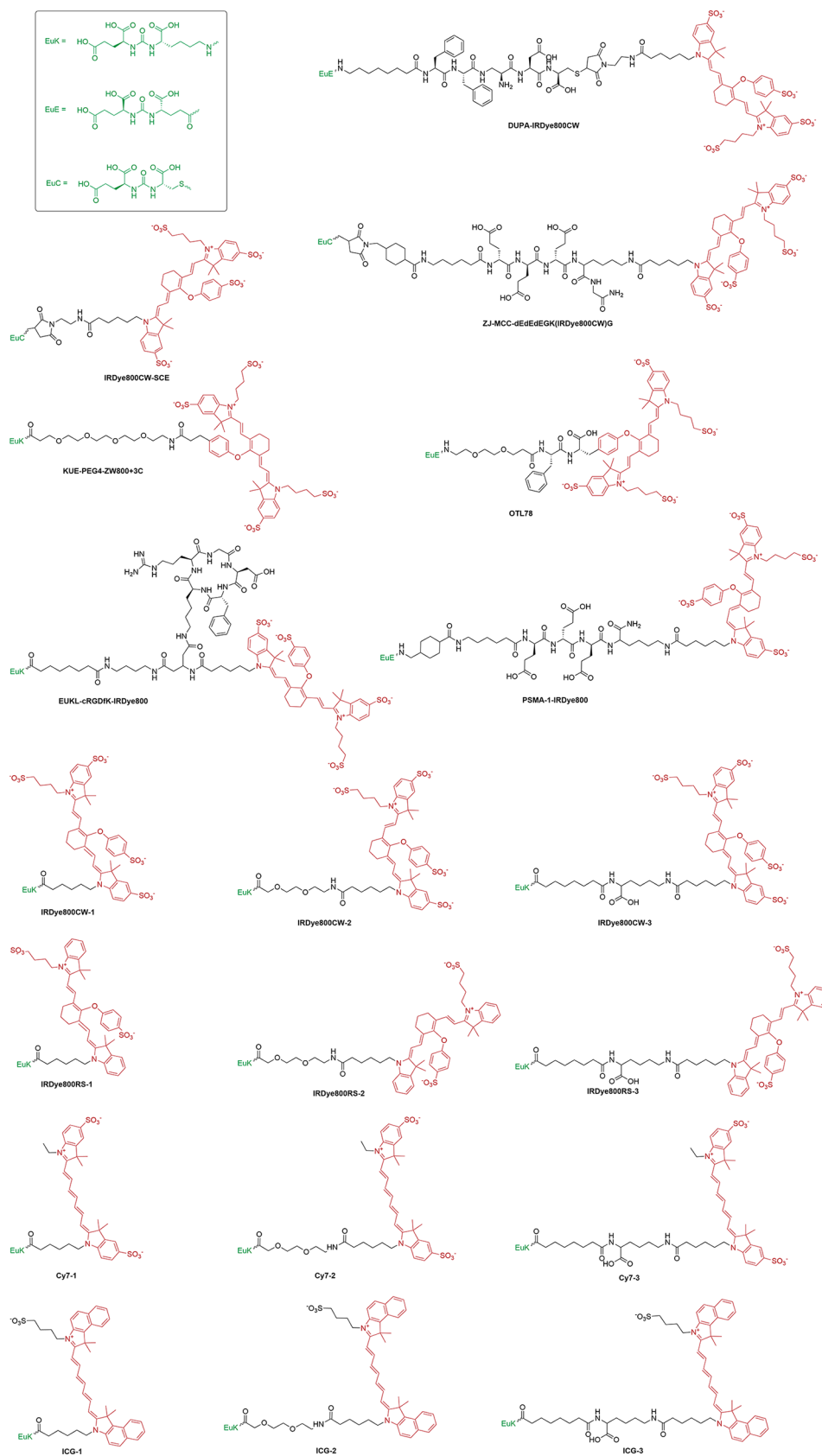
[a]Targeting vector (green) and imaging label (red) were colored accordingly.

By standardizing the EuK targeting vector and Phe-Phe-Dap-Asp-Cys-maleimido-2-aminoethyl spacer, Kelderhouse et al.[46] were able to report the impact that the fluorophores Dylight 680 and AlexaFluor 647 have on PSMA affinity (**DUPA-Dylight 680**
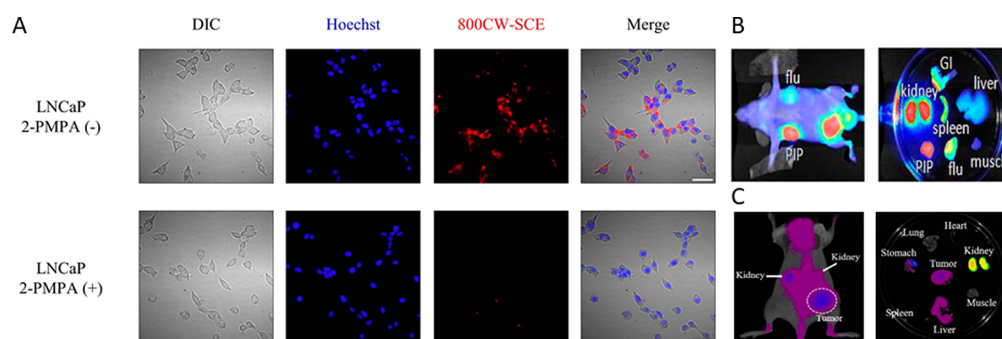
Figure 3. (A) In vitro uptake of **IRDye800CW-SCE** in PSMA-positive LNCaP cells (top) with blocking by 2-PMPA (bottom) (adapted from Matusoka et al.[104] with permission from Elsevier). Example of in vivo imaging and typical biodistribution for (B) **IRDye800CW-1** (adapted from Chen et al.)[101] and (C) **Cy5.5(SO₃⁻)₄-EuK** (adapted from Kwon et al.)[103]

k_D = 33 nM, **DUPA-Alexa Fluor 647** k_D = 4.5 nM). These findings indicated that the fluorophore exerts an influence, but due to a lack of additional data, it is difficult to assess which exact feature of the chemical structure causes this influence.

The influence of spacers was studied for analogs that make use of Cy5.5-tetrakissulfonate by direct comparison.[101] This study indicated that introducing a spacer has a positive effect on the affinity (from k_i = 90 ± 40 pM for **Cy5.5−1** to k_i = 50 ± 20 pM for **Cy5.5−2** and **Cy5.5−3**), but that variations in spacer type predominantly affected the lipophilicity (**Cy5.5−2** LogP = −1.08 to **Cy5.5−3**, LogP = 3.00). Fluorescence imaging results suggested that tumor uptake is increased when the spacers are elongated. Dimerization studies by Kwon et al. underlined the influence of the spacer on the lipophilicity, but also suggested that increasing the number of targeting moieties has minimal impact on the affinity when comparing **Cy5.5(SO₃⁻)₄-EuK** (LogP = −1.36, k_i = 0.6 ± 0.1 nM) with **Cy5.5(SO₃⁻)₄-(EuK)₂** (LogP = −0.33, k_i = 0.1 ± 0.0 nM) and (**Cy5.5(SO₃⁻)₄-4-(aminomethyl)benzoic acid-(EuK)₂**; LogP = 1.32, k_i = 0.4 ± 0.1 nM)[102] A follow-up study showed similar effects on the lipophilicity, but the bi-2-nitroimidazole-containing spacer seemed to limit the affinity.[103] Surprisingly, this chemical alteration did not have a clear impact on the fluorescence imaging findings.

Near-Infrared Fluorescent PSMA-Targeted Tracers. For fluorescence-guided surgery applications, near-infrared Cy7 analogs have been most commonly employed. For the compounds **KUE-PEG₄-ZW800 + 3C**,[105] **IRDye800CW-SCE**,[104] **ZJ-MCC-dEdEdEGK(IRDye800CW)G**,[106] and **EUKL-cRGDfK-IRDye800**[107] the affinity has not been reported, despite the availability of in vivo data suggesting that the compounds could be used to image PSMA-positive lesions. **DUPA-IRDye800CW** has an affinity of k_D = 12 nM, but no in vivo quantification was provided.[46] Individual studies with **OTL78** (LogP = 1.19, k_D = 4.7 nM)[108] and **PSMA-1-IRDye800** (LogP = −2.14, IC_{50} = 1.5 nM)[99] provide promising in vivo findings, but further comparison is hampered by the fact that a reference compound has not been assessed and the chemical composition varies (Table 3, Scheme 3).

By varying spacers and fluorophores, Chen et al.[101] examined how these molecular traits impacted tracer performance. For the fluorophores IRDye800CW, IRDye800RS, and indocyanine green (ICG), the PSMA affinity was highest with the longest Ahx-Lys spacer (k_i = 20, 4, and 5 pM, respectively), indicating that steric hindrance is reduced when a longer spacer is used. Cy7 displayed the highest affinity without the use of a spacer (k_i = 1 pM), suggesting this fluorophore yields little steric

hindrance. No general trends could be inferred from in vivo fluorescence imaging findings or lipophilicity. During in vivo imaging, the fluorescence signal of the IRDye800CW analogs was substantially higher than that of the other analogs. This finding is surprising, as the brightness of Cy7 analogs generally does not differ to such an extent.[109]

Studies that compared different tracer designs under the same conditions allowed for the isolation of general performance trends; not only does the length of the spacer play a role, but its composition also affects affinity. Furthermore, the structure of the fluorophore clearly impacts the tracer performance, e.g., steric hindrance in the secondary binding pocket.

Hybrid Tracers for PSMA. The beneficial traits of both radio- and fluorescent guidance can be integrated by creating hybrid tracers that incorporate a radiolabel and a fluorophore in a single molecule.[110] To date, small-molecule hybrid PSMA-targeted tracers have only been reported in the preclinical setting. Next to structural differences (fluorophore, spacer), different radioisotopes have been included. (Table 4, Scheme 4, Figure 4).

The first hybrid PSMA-targeted tracer design, **IRDye800CW-Lys-DOTA-Gly-urea-Lys**, has been introduced by Banerjee et al.[111] Here, both IRDye800CW and DOTA (to chelate ¹¹¹In) were conjugated to a distal EuK moiety using a Lys-Lys-Suberic acid backbone, a design that is in line with the multifunctional single-attachment point (MSAP) principle coined by Josephson et al.[112] Although this particular spacer design does not seem to actively promote binding in the secondary binding pocket, but rather aims to minimize steric hindrance by the fluorophore, a high affinity was reported for **IRDye800CW-Lys-DOTA-Gly-urea-Lys** (k_i = 1.2 ± 0.1 nM). SPECT imaging showed clear tumor visualization and in vivo biodistribution data (%ID/g assessment at 0.1 nmol) indicated tumor-to-background ratios in the range of 11−37 at time points between 1−24 h. Fluorescence imaging at the same dose (but different imaging time points) allowed for clear tumor visualization.[111] The same MSAP design concept was later used to introduce a bisulfonated cyanine pentamethine (−(SO₃)Cy5(SO₃−) fluorophore and DOTAGA chelate to a D-(3-iodo)Tyr-D-(3-iodo)Tyr spacer optimized for secondary binding,[48] yielding **⁶⁸Ga-PSMA I&F**.[75] The high affinity of this tracer (IC_{50} = 10.5 ± 2.7 nM) translated to a tumor-to-background ration of 9 %ID/g (0.2 nmol) and tumor visualization using SPECT imaging (0.2 nmol) and fluorescence imaging (at 2 nmol) using a customized Firefly laparoscope.

Baranski et al.[113] have applied a design concept wherein the HBED-CC chelate was used to link the EuK binding moiety with

Table 4. PSMA-Targeted Hybrid Tracers for Image-Guided Surgery

compound	receptor affinity (competitor)	tumor-to-background (time point, cell line, background tissue)	kidney-to-tumor (time point, cell line)	injected dose	biodistribution; time point	clearance pathway (time point, uptake clearance organs)	half-life	lipophilicity	plasma protein binding	optimized for entrance funnel?	imaging label (molecular weight)	imaging signature(s)
IRDye800CW-Lys-DOTA-Gly-urea-Lys[111]	K_i = 1.2 ± 0.1 (Not described)	11.58, 19.00, 18.22, 36.50 (1, 2, 5, 24 h, PC3-PIP, muscle)	7.48, 7.29, 7.38, 3.29 (1, 2, 5, 24 h, PC3-PIP)	0.1 nmol (370 MBq/nmol)	Yes; 1, 2, 5, 24 h	Renal (1 h, kidneys 104 ± 9.4%ID/g; liver 2.4 ± 0.1%ID/g; 2 h, kidneys 97.1 ± 13.0%ID/g, liver 2.2 ± 0.0%ID/g, 5 h, kidneys 121.7 ± 21.6%ID/g, liver 3.2 ± 1.2%ID/g 24 h, kidneys 48.1 ± 17.7%ID/g, liver 3.1 ± 0.4%ID/g)	$t_{1/2, rad}$ = 67 h	LogP = 0.12[a]	Data not provided	Yes	DOTAGA, [111]In (387 g/mol); IRDye800CW (983 g/mol)	γ (Eγ = 171.3, 245.4 keV); λabs = 774 nm, λex = 789 nm
^{68}Ga-PSMA I&F[75]	IC50 = 10.5 ± 2.7 nM ((1-BA)-KuE)	9.00 (1 h, LNCaP, muscle)	23.56 (1 h, LNCaP)	0.2 nmol (66 MBq/nmol) (2.0 nmol fluorescence imaging)	Yes; 1 h	Renal (1 h, kidneys 105.8 ± 22.7%ID/g; liver 0.9 ± 0.1%ID/g)	$t_{1/2, rad}$ = 1.1 h	LogP = −3.40	94%	Yes	DOTAGA, [68]Ga (459 g/mol); Cy5 (625 g/mol)	γ (Eγ = 511 keV); λabs = 648 nm, λex = 664 nm
[68]Ga-Glu-urea-Lys-HBED-CC-FITC[113]	IC50 = 11.14 ± 1.16 nM (^{68}Ga-EuK[(Ahx)]2-HBED-CC)	1.06 (1 h, PC3-PIP, muscle)	104 (1 h, PC3-PIP)	60 pmol (17–33 MBq/nmol) 0.5 nmol (fluorescence imaging)	Yes; 1 h	Renal (1 h, kidneys 138 ± 39%ID/g; liver 1.7 ± 0.5%ID/g)	$t_{1/2, rad}$ = 1.1 h	logD = −2.98 ± 0.09	Data not provided	Yes[d]	HBED-CC, [68]Ga (499 g/mol); Fluorescein (346 g/mol)	γ (Eγ = 511 keV); λabs = 494 nm, λex = 512 nm
[68]Ga-Glu-urea-Lys-HBED-CC-AlexaFluor488[113]	IC50 = 13.32 ± 0.83 nM (^{68}Ga-EuK[(Ahx)]2-HBED-CC)	1.35 (1 h, PC3-PIP, muscle)	69 (1 h, PC3-PIP)	60 pmol (17–33 MBq/nmol) 0.5 nmol (fluorescence imaging)	Yes; 1 h	Renal (1 h, kidneys 125 ± 32%ID/g; liver 1.0 ± 0.3%ID/g)	$t_{1/2, rad}$ = 1.1 h	logD = −2.01 ± 0.39	Data not provided	Yes[d]	HBED-CC, [68]Ga (499 g/mol); AlexaFluor488 (505 g/mol)	γ (Eγ = 511 keV); λabs = 490 nm, λex = 525 nm
[68]Ga-Glu-urea-Lys-HBED-CC-IRDye800CW[113]	IC50 = 24.54 ± 5.70 nM (^{68}Ga-EuK[(Ahx)]2-HBED-CC)	1.15, 4.05, 12.88 (1, 2, 6 h, PC3-PIP, muscle)	63.78, 15.11, 24.35 (1, 2, 6 h, PC3-PIP)	60 pmol (17–33 MBq/nmol) 0.5 nmol (fluorescence imaging)	Yes; 1, 2, 6 h	Renal (1 h, kidneys 205 ± 56%ID/g; liver 2.8 ± 0.5%ID/g, 2 h, kidneys 120 ± 5.1%ID/g, liver 1.2 ± 0.1, 6 h, kidneys 160 ± 28%ID/g, liver 1.0 ± 0.2)	$t_{1/2, rad}$ = 1.1 h	logD = −2.21 ± 0.36	Data not provided	Yes[d]	HBED-CC, [68]Ga (499 g/mol); IRDye800CW (983 g/mol)	γ (Eγ = 511 keV); λabs = 774 nm, λex = 789 nm
[68]Ga-Glu-urea-Lys-HBED-CC-DyLight800[113]	IC50 = 21.41 ± 1.90 nM (^{68}Ga-EuK[(Ahx)]2-HBED-CC)	1.46 (1 h, PC3-PIP, muscle)	52.11 (1 h, PC3-PIP)	60 pmol (17–33 MBq/nmol) 0.5 nmol (fluorescence imaging)	Yes; 1 h	Renal (1 h, kidneys 221 ± 24%ID/g; liver 6.2 ± 1.1%ID/g)	$t_{1/2, rad}$ = 1.1 h	logD = −2.95 ± 0.03	Data not provided	Yes[d]	HBED-CC, [68]Ga (499 g/mol); DyLight800 (unknown)	γ (Eγ = 511 keV); λabs = 770 nm, λex = 794 nm
[99m]Tc-EuK-Cy5-mas3[114]	IC50 = 175.3 ± 61.6 nM ((I-BA)-KuE)	18.95 ± 14.66 (2 h, LNCaP, muscle)	2.99 (2 h, LNCaP)	1 nmol (40 MBq/nmol)	Yes; 2 h	Renal (2 h, kidneys 9.0 ± 5.6%ID/g; liver 1.8 ± 0.8%ID/g)	$t_{1/2, rad}$ = 6.5 h	LogP = −2.13 ± 0.10	88%	Yes	mas3, [99m]Tc (408 g/mol); Cy5 (523 g/mol)	γ (Eγ = 140.5 keV); λabs = 648 nm, λex = 664 nm
[99m]Tc-EuK-(SO3)Cy5-mas3[114]	IC50 = 19.2 ± 5.8 nM ((1-BA)-KuE)	5157 ± 949 (2 h, LNCaP, muscle)	1.20 (2 h, LNCaP)	1 nmol (40 MBq/nmol)	Yes; 2 h	Renal (2 h kidneys 18.4 ± 8.5%ID/g; liver 0.6 ± 0.5%ID/g)	$t_{1/2, rad}$ = 6.5 h	LogP = −2.86 ± 0.05	85%	Yes	mas3, [99m]Tc (408 g/mol); Cy5 (602 g/mol)	γ (Eγ = 140.5 keV); λabs = 648 nm, λex = 664 nm
[99m]Tc-EuK-Cy5(SO3)-mas3[114]	IC50 = 118.8 ± 117.4 nM ((I-BA)-KuE)	0.46 ± 0.28 (2 h,)	0.00 (2 h, LNCaP)	1 nmol (40 MBq/nmol)	Yes; 2 h	Renal (2h kidneys 10.5 ± 12.8%ID/g, liver 0.5 ± 0.1%ID/g)	$t_{1/2, rad}$ = 6.5 h	LogP = −2.70 ± 0.01	87%	Yes	mas3, [99m]Tc (408 g/mol); Cy5 (602 g/mol)	γ (Eγ = 140.5 keV); λabs = 664 nm

Table 4. continued

compound	receptor affinity (competitor)	tumor-to-background (time point, cell line, background tissue)	kidney-to-tumor (time point, cell line)	injected dose	biodistribution; time point	clearance pathway (time point, uptake clearance organs)	half-life	lipophilicity	plasma protein binding	optimized for entrance funnel?	imaging label (molecular weight)	imaging signature(s)
^{99m}Tc-EuK-(Ar)Cy5-mas$_3$[114]	IC$_{50}$ = 113.1 ± 35.9 nM ((I-BA)-KuE)	172 ± 84.95 (2 h, LNCaP, muscle)	4.51 (2 h, LNCaP)	1 nmol (40 MBq/nmol)	Yes; 2 h	Renal (2 h, kidneys 15.6 ± 20.0%ID/g, liver 3.3 ± 2.2%ID/g)	$t_{1/2, rad}$ = 6.5 h	LogP = −1.75 ± 0.10	91%	Yes	mas$_3$, ^{99m}Tc (408 g/mol); Cy5 (612 g/mol)	γ ($E\gamma$ = 140.5 keV); λ_{abs} = 648 nm, λ_{ex} = 664 nm
^{99m}Tc-EuK-Cy5(Ar)-mas$_3$[114]	IC$_{50}$ = 164.4 ± 76.9 nM ((I-BA)-KuE)	5.79 ± 0.86 (2 h, LNCaP, muscle)	2.87 (2 h, LNCaP)	1 nmol (40 MBq/nmol)	Yes; 2 h	Renal (2 h, kidneys 11.9 ± 12.3%ID/g, liver 9.6 ± 6.8%ID/g)	$t_{1/2, rad}$ = 6.5 h	LogP = −1.84 ± 0.06	89%	Yes	mas$_3$, ^{99m}Tc (408 g/mol); Cy5 (612 g/mol)	γ ($E\gamma$ = 140.5 keV); λ_{abs} = 648 nm, λ_{ex} = 664 nm
^{18}F-(SO$_3$)Cy3(SO$_3$)-EuK[115]	EC$_{50}$ = 10.3 ± 0.7 nM (Unlabeled (SO$_3$)Cy3(SO$_3$)-EuK)	128 (2 h, PC3-PIP, blood)	0.06 (2 h, PC3-PIP)	2.5 nmol (7.0 ± 1.9 MBq/nmol)	Yes; 2 h	Renal (2 h, kidneys 1.0 ± 0.5%ID/g, liver 0.1 ± 0.0%ID/g)	$t_{1/2, rad}$ = 1.8 h	LogP = 1.02[a]	Data not provided	No	^{18}F (278 g/mol); Cy3 (682 g/mol)	β ($E_{max}\beta^+$ = 634 keV); λ_{abs} = 550 nm, λ_{ex} = 570 nm

^{a}Values were calculated by using ChemAxon's Chemicalize plugin. ^{b}Estimated from graph. ^{c}Estimated from scale bar. AU = arbitrary units. ^{d}No spacer as opposed to parental compound PSMA-11.[78]

Scheme 4. Chemical Structures of Hybrid Tracers for PSMA-Targeted Image-Guided Surgery[a]
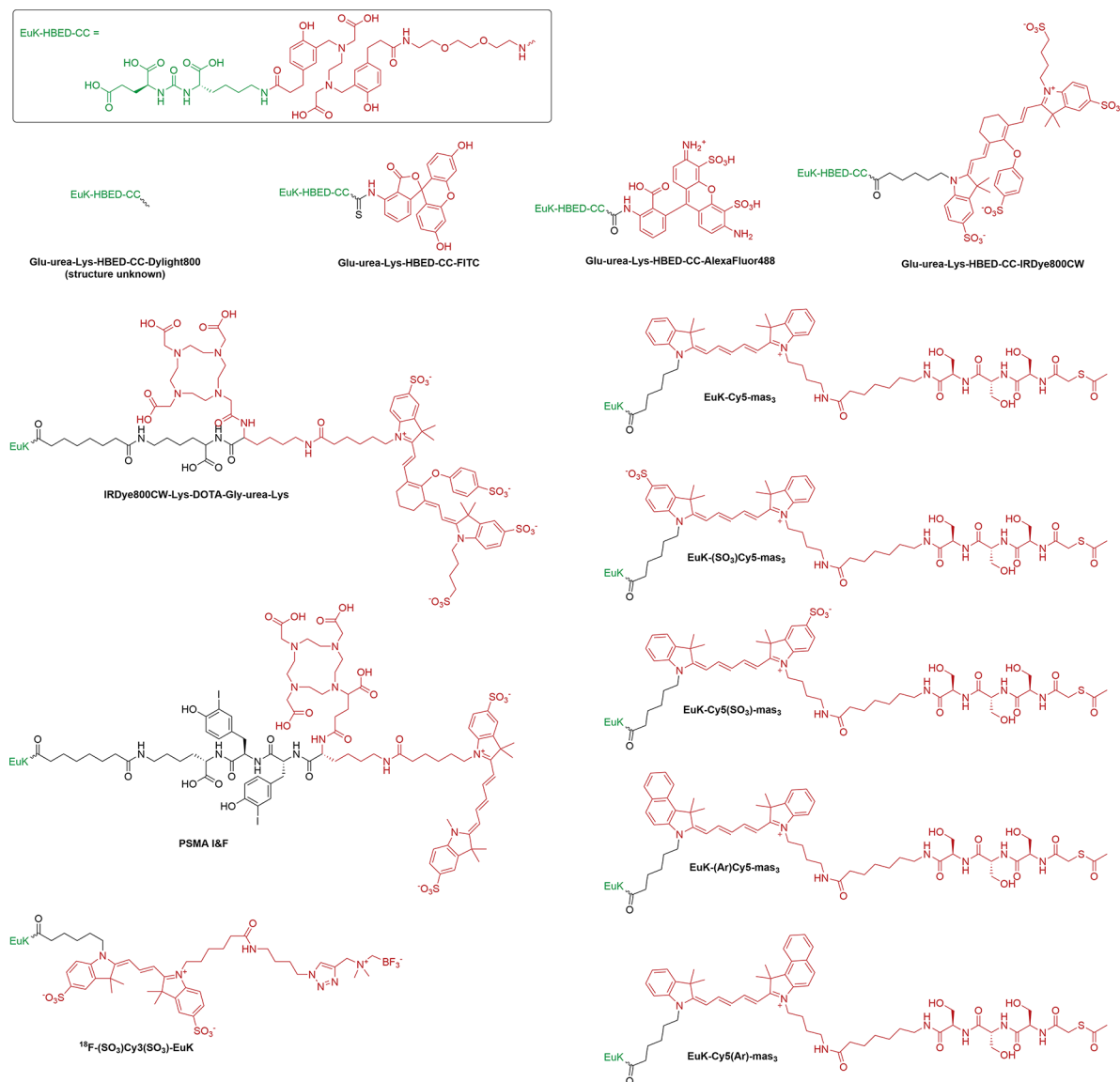
[a]Targeting vector (green) and imaging label (red) were colored accordingly.
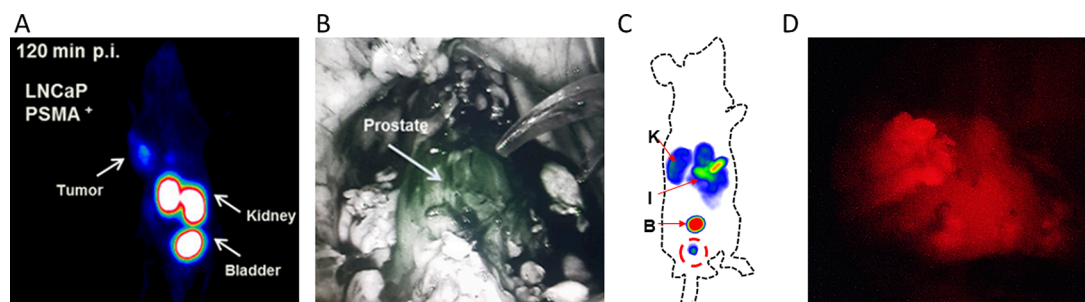

Figure 4. (A) Maximum-intensity projections of small-animal PET imaging of athymic nude mice bearing LNCaP tumors using 0.5 nmol ^{68}Ga-HBED-CC-IRDye800CW. (B) Use of **HBED-CC-IRDye800CW** in vivo for fluorescence imaging with a Da Vinci Firefly laparoscope (1 mg, 30 μg/kg; both adapted from Baranski et al.,[113] in JNM). (C) Maximum-intensity projections of small-animal SPECT imaging of BALB/c nude mice bearing LNCaP tumors using 1.0 nmol ^{99m}Tc-EuK-(SO3)Cy5-COOH (adapted from Hensbergen et al. in JNM).[114] (D) Use of ^{99m}Tc-EuK-(SO3)Cy5-COOH (100 μg, 2.85 μg/kg) for in vivo fluorescence imaging with a prototype Karl Storz camera that allows Cy5 imaging.

a PEG spacer containing a variety of fluorophores. This ^{68}Ga-based hybrid design was derived from ^{68}Ga-PSMA-11 (Table 1, Scheme 1),[78] but the 6-aminohexanoic acid spacer between

HBED-CC and EuK was removed. Varying the fluorophore (FITC, AlexaFluor488, IRDye800CW, or DyLight800) did not significantly impact the logD values [(2.01 ± 0.39)−(2.98 ±

Table 5. Differences between Fluorescence- and Radioactivity-Based Image-Guided Surgery

	fluorescence	radioactivity
Spatial resolution	μm–mm's	>2 mm
Signal display	Video rate	Only numeric/acoustic (γ-probe) or static image (γ camera)
Acquisition time	<50 ms	>500 ms (γ-probe), multiple seconds (γ camera)
Compatibility with microscopic tissue evaluation	Fluorescence microscopy (<μm resolution)	Autoradiography (>mm)
Biodistribution	Qualitative (image intensity only; impacted by autofluorescence and tissue-based signal attenuation)	Quantitative (%ID/g)
Signal penetration depth through tissue	<10 mm	>10 mm
Noninvasive whole-body imaging (surgical roadmap)	n.a.	2D scintigraphy/3D (e.g., SPECT/CT, PET/CT)

0.09)], but did impact the PSMA affinity (IC_{50} = 11.14 ± 1.16, 13.32 ± 0.83, 24.54 ± 5.70, and 21.41 ± 1.90 nM, respectively). Quantitative biodistribution using the ^{68}Ga isotope (%ID/g assessment at 60 pmol) at 1 h p.i. showed that the structural variations also extended to renal retention (138 ± 39, 125 ± 32, 205 ± 56, and 221 ± 24%ID/g, respectively), which could impact the performance of tumor imaging as discussed previously. This particular comparison allows for the isolation of the influence that a fluorophore exerts on tracer performance. In mice, **^{68}Ga-Glu-urea-Lys-HBED-CC-IRDye800CW** could be used to identify PSMA-positive tumors with small-animal PET (Figure 4A; 0.5 nmol) or fluorescence imaging (0.5 nmol). Interestingly, basal prostate uptake of **Glu-urea-Lys-HBED-CC-IRDye800CW** in healthy pigs (1 mg, 30 μg/kg) was evaluated using a Da Vinci Firefly laparoscope (Figure 4B).[113]

Alternatively, the use of cyanine fluorophores as spacers has been explored. By using the fluorophore as spacer but keeping the primary targeting vector and mas$_3$ chelate consistent, it became possible to systematically study if and how a custom bifunctional Cy5 fluorophore (i.e., −Cy5−, −(SO$_3$)Cy5−, −Cy5(SO$_3$)−, −(Ar)Cy5−, and −Cy5(Ar)−) could influence secondary binding to the amphipathic entrance funnel.[114] Affinities were greatly impacted by the fluorophore design: of the five fluorophores studied only −(SO$_3$)Cy5− showed IC_{50} < 100 nM (**EuK-(SO$_3^-$)Cy5-mas$_3$**, IC_{50} = 19.2 ± 5.8 nM). These results imply that the presence and location of an anionic sulfonate moiety on the fluorophore influence the affinity for PSMA. At 2 h p.i. using a dose of 1 nmol, **^{99m}Tc-EuK-(SO$_3^-$)Cy5-mas$_3$** displayed a relatively low renal retention (18.4 ± 8.5%ID/g), as well as high tumor-to-muscle and good kidney-to-tumor ratios (Figure 4C, Table 4). This compound is currently under evaluation in a healthy pig model where it allows accurate prostate delineation using a microdosing regimen (100 μg, 2.85 μg/kg; Figure 4D). Kommidi et al.[115] have used the commercially available HOOC-(SO$_3$)Cy3(SO$_3$)-COOH to create **^{18}F-(SO$_3$)Cy3(SO$_3$)-EuK**. In line with the above findings, this compound has a high affinity (EC_{50} = 10.3 ± 0.7 nM) and tumors could be clearly visualized using small-animal PET imaging. Quantitative biodistribution studies indicated a high tumor uptake (tumor-to-blood ratio = 128) and low renal retention (kidney-to-tumor ratio 0.06 at 2 h) using a dose of 2.5 nmol. Here, it should be noted the fact that **^{18}F-(SO$_3$)Cy3-(SO$_3$)-EuK** is radiohalogenated, which implies it has a reduced amount of charges compared to radiometalated ligands, and as such can influence renal accumulation and/or clearance.[116]

In summary, three types of hybrid tracer designs have been reported: (1) MSAP, (2) chelate-spacer-based, and (3) fluorophore-spacer-based. In general, these studies indicate

that the affinity of the hybrid tracers is impacted by the addition of a fluorophore. This effect, however, is most substantial when the fluorophore resides within the secondary binding pocket. In some cases, the dose used for the biodistribution in%ID/g was different from the dose used for fluorescence imaging, making it difficult to assess in vivo performance for the latter application.

■ DISCUSSION

By combining the binding characteristics of PSMA with the clinical need for accurate and sensitive detection of PSMA-positive lesions during PCa surgery, a general perspective could be created for the evaluation of the three families of PSMA-targeted tracers for image-guided surgery (i.e., radioactive, fluorescent, and hybrid). This overview suggests the "low-hanging fruit" in PSMA tracer design has been picked by incorporating off-the-shelf imaging labels and spacers on a well-known targeting moiety. Although the majority of PSMA-targeted tracers designed for image-guided surgery applications are fluorescent (Tables 2, 3, Schemes 2, 3) or hybrid (Table 4, Scheme 4) of nature, only radiotracers (Table 1, Scheme 1) have been reported in clinical trials so far. Hence, it does not seem that we are currently getting the most out of PSMA-targeted tracer developments for image-guided surgery purposes.

Published clinical data with ^{99m}Tc-PSMA I&S focuses on the positive influence image-guided surgery has on the resection of tumor-positive LNs in the salvage setting (after staging with PSMA−PET).[57,96] Due to the lack of reports that describe the use of these radiotracers in primary cancer resection, it is difficult to judge the potential of PSMA-targeted image guidance for this application. Most likely, resection of PSMA-positive LNs in the primary setting will be equally as effective as in a salvage setting, but given the overall renal clearance and high renal accumulation of the PSMA-targeted tracers reported, the ability to detect primary tumor margins is likely more reliant on the chemical design of the tracer.

We have attempted to comprehend the requirements for the chemical design of a high-end tracer for PSMA-targeted image-guided surgery, but comparative interstudy performance assessment was impaired by a number of features: (1) lack of a standardized methodology for affinity assessment (k_i, k_D, IC_{50}; in some cases picomolar range affinities have been reported, while comparative studies yield a lower affinity (nanomolar range) for similar designs); (2) although it is known that the applied dose influences the biodistribution of PSMA-targeted tracers,[117,118] large variations in dose have been reported between, e.g., fluorescence- and radioactivity-based studies (0.1−1 nmol for radio- and hybrid tracers, 1−10 nmol for fluorescent tracers; Table 1−3); (3) differences in time points of

imaging (1–120 h; Table 1–3), combined with the biological clearance profiles of individual tracers, are common and are likely to impact the intensity of background signals; (4) missing quantitative biodistribution data (%ID/g) for fluorescence tracers (Table 4) makes it particularly challenging to place the reported preclinical findings in perspective to the PSMA–PET tracers that are currently used for staging of patients; (5) use of different animal/tumor models complicates a direct comparison based on tumor uptake values—it has been shown that the use of different tumor models can increase the tumor uptake by almost 3-fold,[116] it might cause one to wonder how accurately proof-of-concept studies in mice represent the challenges encountered during PCa surgery; (6) utility of radioactive and fluorescent signatures for imaging is intrinsically different, further complicating a comparison of the findings (Table 5).

Despite the hampering of interstudy comparisons, a number of manuscripts cited in this review (one regarding radiotracers, four regarding fluorescent tracers and two regarding hybrid tracers) allowed for a structural intrastudy comparison of different tracer analogs. These studies therefore complement the existing radiochemistry literature on PSMA-targeted tracer refinement.[5] Key performance characteristics could be inferred from these combined data, e.g., that the spacer can be used to influence the binding to the secondary pocket and/or to limit steric hindrance from "bulky" imaging labels.[102,103] Hereby the molecular features of different fluorophores exert a different impact on affinity and tracer kinetics, similar to what has been reported for chelates/radiolabels.[62,63] The influence of the molecular composition of fluorophores was largest when short spacers were used (meaning the fluorophores were placed in the amphipathic entrance funnel),[101] or when the fluorophores were purposely exploited as spacers.[113,114] In the secondary binding pocket, cyanine fluorophore structures with sulfonates instead of additional aromatic rings yielded the highest affinity. Furthermore, it is interesting to note that a study by Wang et al. underlines that Cy5 fluorophores are not always outperformed by Cy7 analogs.[99]

Besides strides that can be taken in optimization of the chemical design, clinical translation of fluorescent tracers is also affected by the sensitivity of detection. The translation of radiotracers such as ^{99m}Tc-PSMA I&S was supported by the ability to apply these tracers in a microdosing regime, a concept that limits toxicity and eases the clinical translation of radiotracers.[119] Despite clinical data indicating that fluorescence-guided surgery might also be feasible adhering to the microdosing principle,[73,120,121] as has also been suggested for PSMA using a porcine model (Figure 4D), the application of microdosing remains controversial in the field of fluorescence-guided surgery.[122] It is certain, however, that intraoperative identification of (fluorescent) lesions is less efficient when they contain low tracer concentrations.[73] Other than PSMA–PET studies reporting on a >2 mm size limit for lesion identification,[55] little is known about the PSMA concentration on cancer cells in primary or metastatic lesions. Currently, analysis of the PSMA–PET roadmap is one of the clinical selection criteria for the inclusion of patients in PSMA-guided salvage surgery.[20] One might argue that inclusion of quantitative analysis (e.g., SUV) of the lesion is these scans, coupled to quantitative surgical detection and pathological analysis, could in the future help define which PSMA concentration levels are needed to support radio- and/or fluorescence-based lesion identification in a surgical setting.

Given the clinical impact of PSMA-targeted radioguided surgery, the limited insights provided for the in vivo performance of fluorescent PSMA-targeted tracers and literature suggesting that tissue-induced signal attenuation, e.g., as result of a high body mass index, limits the accuracy of fluorescence-guided surgery.[123,124] It is likely that PSMA-targeted tracers incorporating a radiolabel are most promising. Here, the "best-of-both-worlds" scenario offered by hybrid tracers (combination of features in Table 5) seems to provide a logical means to support preoperative imaging and radioguided surgery, while at the same time satisfying the surgeon's desire for fluorescence guidance.[110]

Next to the small-molecule PSMA-tracers, antibody-based efforts are also explored for this molecular target.[125−129] In the future, these different tracer designs can jointly address PSMA-based resections in PCa and given the biology of PSMA, they can possibly also guide resections in other cancers. When PCa is PSMA-negative or PSMA-expression is low, other molecular targets may be used for surgical guidance, e.g., the fibroblast activation protein[130] or gastrin-releasing peptide receptor.[131]

CONCLUSION

Different PSMA-targeted tracers have been reported for the field of PSMA-targeted image-guided surgery. When comparing the reported radio-, fluorescent-, and hybrid PSMA-targeted tracers it becomes evident that (1) radiotracers have already created clinical impact, (2) fluorescent tracers are most abundant but are used at a relatively high dose and the preclinical studies lack pharmacokinetic assessment, and (3) hybrid tracers provide the potential to complement the beneficial values of radiotracers with fluorescence guidance.

AUTHOR INFORMATION

Corresponding Author
*E-mail: f.w.b.van_leeuwen@lumc.nl. Phone: +31715266029.
ORCID ⊙
Tessa Buckle: 0000-0003-2980-6895
Fijs W. B. van Leeuwen: 0000-0002-6844-4025
Notes
The authors declare the following competing financial interest(s): F. W. B. van Leeuwen is Chief Innovation Officer at ORSI Academy, and H.-J. Wester is founder and shareholder of Scintomics GmbH.

ACKNOWLEDGMENTS

REFERENCES

(1) Bray, F., Ferlay, J., Soerjomataram, I., Siegel, R. L., Torre, L. A., and Jemal, A. (2018) Global cancer statistics 2018: GLOBOCAN estimates of incidence and mortality worldwide for 36 cancers in 185 countries. *Ca-Cancer J. Clin. 68*, 394−424.

(2) Silver, D. A., Pellicer, I., Fair, W. R., Heston, W. D., and Cordon-Cardo, C. (1997) Prostate-specific membrane antigen expression in normal and malignant human tissues. *Clin. Cancer Res. 3*, 81−5.

(3) Jin, J. K., Dayyani, F., and Gallick, G. E. (2011) Steps in prostate cancer progression that lead to bone metastasis. *Int. J. Cancer 128*, 2545−61.

(4) Maurer, T., Eiber, M., Schwaiger, M., and Gschwend, J. E. (2016) Current use of PSMA-PET in prostate cancer management. *Nat. Rev. Urol. 13*, 226−35.

(5) Schwarzenböck, S. M., Rauscher, I., Blümel, C., Fendler, W. P., Rowe, S. P., Pomper, M. G., Afshar-Oromieh, A., Herrmann, K., and Eiber, M. (2017) PSMA Ligands for PET Imaging of Prostate Cancer. *J. Nucl. Med. 58*, 1545−1552.

(6) Afshar-Oromieh, A., Avtzi, E., Giesel, F. L., Holland-Letz, T., Linhart, H. G., Eder, M., Eisenhut, M., Boxler, S., Hadaschik, B. A., Kratochwil, C., et al. (2015) The diagnostic value of PET/CT imaging with the (68)Ga-labelled PSMA ligand HBED-CC in the diagnosis of recurrent prostate cancer. *Eur. J. Nucl. Med. Mol. Imaging 42*, 197−209.

(7) Afshar-Oromieh, A., Sattler, L. P., Mier, W., Hadaschik, B. A., Debus, J., Holland-Letz, T., Kopka, K., and Haberkorn, U. (2017) The Clinical Impact of Additional Late PET/CT Imaging with (68)Ga-PSMA-11 (HBED-CC) in the Diagnosis of Prostate Cancer. *J. Nucl. Med. 58*, 750−755.

(8) Eiber, M., Maurer, T., Souvatzoglou, M., Beer, A. J., Ruffani, A., Haller, B., Graner, F. P., Kubler, H., Haberkorn, U., Eisenhut, M., et al. (2015) Evaluation of Hybrid (68)Ga-PSMA Ligand PET/CT in 248 Patients with Biochemical Recurrence After Radical Prostatectomy. *J. Nucl. Med. 56*, 668−74.

(9) Fendler, W. P., Calais, J., Eiber, M., Flavell, R. R., Mishoe, A., Feng, F. Y., Nguyen, H. G., Reiter, R. E., Rettig, M. B., Okamoto, S., et al. (2019) Assessment of ^{68}Ga-PSMA-11 PET Accuracy in Localizing Recurrent Prostate Cancer: A Prospective Single-Arm Clinical Trial. *Jama Oncol 5*, 856−863.

(10) Rauscher, I., Duwel, C., Haller, B., Rischpler, C., Heck, M. M., Gschwend, J. E., Schwaiger, M., Maurer, T., and Eiber, M. (2018) Efficacy, Predictive Factors, and Prediction Nomograms for (68)Ga-labeled Prostate-specific Membrane Antigen-ligand Positron-emission Tomography/Computed Tomography in Early Biochemical Recurrent Prostate Cancer After Radical Prostatectomy. *Eur. Urol. 73*, 656−661.

(11) Maurer, T., Gschwend, J. E., Rauscher, I., Souvatzoglou, M., Haller, B., Weirich, G., Wester, H.-J., Heck, M., Kubler, H., Beer, A. J., et al. (2016) Diagnostic Efficacy of (68)Gallium-PSMA Positron Emission Tomography Compared to Conventional Imaging for Lymph Node Staging of 130 Consecutive Patients with Intermediate to High Risk Prostate Cancer. *J. Urol. 195*, 1436−1443.

(12) Benešová, M., Schäfer, M., Bauder-Wüst, U., Afshar-Oromieh, A., Kratochwil, C., Mier, W., Haberkorn, U., Kopka, K., and Eder, M. (2015) Preclinical Evaluation of a Tailor-Made DOTA-Conjugated PSMA Inhibitor with Optimized Linker Moiety for Imaging and Endoradiotherapy of Prostate Cancer. *J. Nucl. Med. 56*, 914−20.

(13) Weineisen, M., Schottelius, M., Simeček, J., Baum, R. P., Yıldız, A., Beykan, S., Kulkarni, H. R., Lassmann, M., Klette, I., Eiber, M., et al. (2015) [68]Ga- and ^{177}Lu-Labeled PSMA I&T: Optimization of a PSMA-Targeted Theranostic Concept and First Proof-of-Concept Human Studies. *J. Nucl. Med. 56*, 1169−76.

(14) Wester, H.-J., and Schottelius, M. (2019) PSMA-Targeted Radiopharmaceuticals for Imaging and Therapy. *Semin. Nucl. Med. 49*, 302−312.

(15) Kupelian, P. A., Potters, L., Khuntia, D., Ciężki, J. P., Reddy, C. A., Reuther, A. M., Carlson, T. P., and Klein, E. A. (2004) Radical prostatectomy, external beam radiotherapy < 72 Gy, external beam radiotherapy > or = 72 Gy, permanent seed implantation, or combined seeds/external beam radiotherapy for stage T1-T2 prostate cancer. *Int. J. Radiat. Oncol., Biol., Phys. 58*, 25−33.

(16) Fossati, N., Wiklund, P., Rochat, C. H., Montorsi, F., Dasgupta, P., Sanchez-Salas, R., Canda, A. E., Piechaud, T., Artibani, W., and Mottrie, A. (2017) Robotic and Open Radical Prostatectomy: The First Prospective Randomised Controlled Trial Fuels Debate Rather than Closing the Question. *Eur. Urol. 71*, 307−308.

(17) Raskolnikov, D., George, A. K., Rais-Bahrami, S., Turkbey, B., Siddiqui, M. M., Shakir, N. A., Okoro, C., Rothwax, J. T., Walton-Diaz, A., Sankineni, S., et al. (2015) The Role of Magnetic Resonance Image Guided Prostate Biopsy in Stratifying Men for Risk of Extracapsular Extension at Radical Prostatectomy. *J. Urol. 194*, 105−111.

(18) van Leeuwen, F. W. B., Winter, A., van Der Poel, H. G., Eiber, M., Suardi, N., Gräfen, M., Wawroschek, F., and Maurer, T. (2019) Technologies for image-guided surgery for managing lymphatic metastases in prostate cancer. *Nat. Rev. Urol. 16*, 159−171.

(19) van Oosterom, M. N., van der Poel, H. G., Navab, N., van de Velde, C. J. H., and van Leeuwen, F. W. B. (2018) Computer-assisted surgery: virtual- and augmented-reality displays for navigation during urological interventions. *Curr. Opin Urol 28*, 205−213.

(20) Maurer, T., Gräfen, M., van der Poel, H., Hamdy, F., Briganti, A., Eiber, M., Wester, H.-J., and van Leeuwen, F. (2019) Prostate-specific membrane antigen guided surgery. *J. Nucl. Med.*.

(21) Derks, Y. H. W., Lowik, D., Sedelaar, J. P. M., Gotthardt, M., Boerman, O. C., Rijpkema, M., Lütje, S., and Heskamp, S. (2019) PSMA-targeting agents for radio- and fluorescence-guided prostate cancer surgery. *Theranostics 9*, 6824−6839.

(22) Maurer, T., van Leeuwen, F. W. B., Schottelius, M., Wester, H.-J., and Eiber, M. (2019) Entering the era of molecular-targeted precision surgery in recurrent prostate cancer. *J. Nucl. Med. 60*, 156−157.

(23) Pastorino, S., Riondato, M., Uccelli, L., Giovacchini, G., Giovannini, E., Duce, V., and Ciarmiello, A. (2019) Toward the discovery and development of PSMA targeted inhibitors for nuclear medicine applications. *Curr. Radiopharm. 12*, 1−17.

(24) Kaittanis, C., Andreou, C., Hieronymus, H., Mao, N., Foss, C. A., Eiber, M., Weirich, G., Panchal, P., Gopalan, A., Zurita, J., et al. (2018) Prostate-specific membrane antigen cleavage of vitamin B9 stimulates oncogenic signaling through metabotropic glutamate receptors. *J. Exp. Med. 215*, 159−175.

(25) Pavlíček, J., Ptáček, J., and Barinka, C. (2012) Glutamate carboxypeptidase II: an overview of structural studies and their importance for structure-based drug design and deciphering the reaction mechanism of the enzyme. *Curr. Med. Chem. 19*, 1300−9.

(26) Rawlings, N. D., and Barrett, A. J. (1997) Structure of membrane glutamate carboxypeptidase. *Biochim. Biophys. Acta, Protein Struct. Mol. Enzymol. 1339*, 247−52.

(27) Perico, M. E., Grasso, S., Brunelli, M., Martignoni, G., Munari, E., Moiso, E., Fracasso, G., Cestari, T., Naim, H. Y., Bronte, V., et al. (2016) Prostate-specific membrane antigen (PSMA) assembles a macromolecular complex regulating growth and survival of prostate cancer cells "in vitro" and correlating with progression "in vivo. *Oncotarget 7*, 74189−74202.

(28) Liu, H., Rajasekaran, A. K., Moy, P., Xia, Y., Kim, S., Navarro, V., Rahmati, R., and Bander, N. H. (1998) Constitutive and antibody-induced internalization of prostate-specific membrane antigen. *Cancer Res. 58*, 4055−60.

(29) Dorff, T. B., Fanti, S., Farolfi, A., Reiter, R. E., Sadun, T. Y., and Sartor, O. (2019) The Evolving Role of Prostate-Specific Membrane Antigen-Based Diagnostics and Therapeutics in Prostate Cancer. *Am. Soc. Clin Oncol Educ Book 39*, 321−330.

(30) Bravaccini, S., Puccetti, M., Bocchini, M., Ravaioli, S., Celli, M., Scarpi, E., De Giorgi, U., Tumedei, M. M., Raulli, G., Cardinale, L., et al. (2018) PSMA expression: a potential ally for the pathologist in prostate cancer diagnosis. *Sci. Rep. 8*, 4254.

(31) Chang, S. S., O'Keefe, D. S., Bacich, D. J., Reuter, V. E., Heston, W. D. W., and Gaudin, P. B. (1999) Prostate-specific membrane antigen is produced in tumor-associated neovasculature. *Clin. Cancer Res. 5*, 2674−2681.

(32) Wright, G. L., Jr., Grob, B. M., Haley, C., Grossman, K., Newhall, K., Petrylak, D., Troyer, J., Konchuba, A., Schellhammer, P. F., and Moriarty, R. (1996) Upregulation of prostate-specific membrane antigen after androgen-deprivation therapy. *Urology 48*, 326−34.

(33) Vaz, S., Hadaschik, B., Gabriel, M., Herrmann, K., Eiber, M., and Costa, D. (2020) Influence of androgen deprivation therapy on PSMA expression and PSMA-ligand PET imaging of prostate cancer patients. *Eur. J. Nucl. Med. Mol. Imaging 47*, 9−15.

(34) Ghosh, A., and Heston, W. D. (2004) Tumor target prostate specific membrane antigen (PSMA) and its regulation in prostate cancer. *J. Cell. Biochem. 91*, 528−39.

(35) Klusák, V., Barinka, C., Plechanovová, A., Mlcochová, P., Konvalinka, J., Rulisek, L., and Lubkowski, J. (2009) Reaction mechanism of glutamate carboxypeptidase II revealed by mutagenesis, X-ray crystallography, and computational methods. *Biochemistry 48*, 4126−38.

(36) Barinka, C., Rovenská, M., Mlcochová, P., Hlouchová, K., Plechanovová, A., Majer, P., Tsukamoto, T., Slusher, B. S., Konvalinka, J., and Lubkowski, J. (2007) Structural insight into the pharmacophore pocket of human glutamate carboxypeptidase II. *J. Med. Chem. 50*, 3267–73.

(37) Barinka, C., Šácha, P., Sklenar, J., Man, P., Bezouška, K., Slusher, B. S., and Konvalinka, J. (2004) Identification of the N-glycosylation sites on glutamate carboxypeptidase II necessary for proteolytic activity. *Protein Sci. 13*, 1627–35.

(38) Hlouchová, K., Barinka, C., Klusák, V., Šácha, P., Mlcochová, P., Majer, P., Rulisek, L., and Konvalinka, J. (2007) Biochemical characterization of human glutamate carboxypeptidase III. *J. Neurochem. 101*, 682–96.

(39) Jackson, P. F., Tays, K. L., Maclin, K. M., Ko, Y. S., Li, W., Vitharana, D., Tsukamoto, T., Störmer, D., Lu, X. C., Wozniak, K., et al. (2001) Design and pharmacological activity of phosphinic acid based NAALADase inhibitors. *J. Med. Chem. 44*, 4170–5.

(40) Majer, P., Jackson, P. F., Delahanty, G., Grella, B. S., Ko, Y. S., Li, W., Liu, Q., Maclin, K. M., Poláková, J., Shaffer, K. A., et al. (2003) Synthesis and biological evaluation of thiol-based inhibitors of glutamate carboxypeptidase II: discovery of an orally active GCP II inhibitor. *J. Med. Chem. 46*, 1989–96.

(41) Kozikowski, A. P., Nan, F., Conti, P., Zhang, J., Ramadan, E., Bzdega, T., Wróblewska, B., Neale, J. H., Pshenichkin, S., and Wróblewski, J. T. (2001) Design of remarkably simple, yet potent urea-based inhibitors of glutamate carboxypeptidase II (NAALADase). *J. Med. Chem. 44*, 298–301.

(42) Barinka, C., Byun, Y., Dusich, C. L., Banerjee, S. R., Chen, Y., Castanares, M., Kozikowski, A. P., Mease, R. C., Pomper, M. G., and Lubkowski, J. (2008) Interactions between human glutamate carboxypeptidase II and urea-based inhibitors: structural characterization. *J. Med. Chem. 51*, 7737–43.

(43) Tykvart, J., Schimer, J., Bařinková, J., Pachl, P., Postova-Slavetinska, L., Majer, P., Konvalinka, J., and Šácha, P. (2014) Rational design of urea-based glutamate carboxypeptidase II (GCPII) inhibitors as versatile tools for specific drug targeting and delivery. *Bioorg. Med. Chem. 22*, 4099–4108.

(44) Wang, H., Byun, Y., Barinka, C., Pullambhatla, M., Bhang, H. E., Fox, J. J., Lubkowski, J., Mease, R. C., and Pomper, M. G. (2010) Bioisosterism of urea-based GCPII inhibitors: Synthesis and structure-activity relationship studies. *Bioorg. Med. Chem. Lett. 20*, 392–7.

(45) Chen, Y., Dhara, S., Banerjee, S. R., Byun, Y., Pullambhatla, M., Mease, R. C., and Pomper, M. G. (2009) A low molecular weight PSMA-based fluorescent imaging agent for cancer. *Biochem. Biophys. Res. Commun. 390*, 624–9.

(46) Kelderhouse, L. E., Chelvam, V., Wayua, C., Mahalingam, S., Poh, S., Kularatne, S. A., and Low, P. S. (2013) Development of tumor-targeted near infrared probes for fluorescence guided surgery. *Bioconjugate Chem. 24*, 1075–80.

(47) Kularatne, S. A., Zhou, Z., Yang, J., Post, C. B., and Low, P. S. (2009) Design, synthesis, and preclinical evaluation of prostate-specific membrane antigen targeted (99m)Tc-radioimaging agents. *Mol. Pharmaceutics 6*, 790–800.

(48) Schottelius, M., Wirtz, M., Eiber, M., Maurer, T., and Wester, H.-J. (2015) [(111)In]PSMA-I&T: expanding the spectrum of PSMA-I&T applications towards SPECT and radioguided surgery. *EJNMMI Res. 5*, 68.

(49) Banerjee, S. R., Foss, C. A., Castanares, M., Mease, R. C., Byun, Y., Fox, J. J., Hilton, J., Lupold, S. E., Kozikowski, A. P., and Pomper, M. G. (2008) Synthesis and evaluation of technetium-99m- and rhenium-labeled inhibitors of the prostate-specific membrane antigen (PSMA). *J. Med. Chem. 51*, 4504–17.

(50) Afshar-Oromieh, A., Zechmann, C. M., Malcher, A., Eder, M., Eisenhut, M., Linhart, H. G., Holland-Letz, T., Hadaschik, B. A., Giesel, F. L., Debus, J., et al. (2014) Comparison of PET imaging with a (68)Ga-labelled PSMA ligand and (18)F-choline-based PET/CT for the diagnosis of recurrent prostate cancer. *Eur. J. Nucl. Med. Mol. Imaging 41*, 11–20.

(51) Fendler, W. P., Weber, M., Iravani, A., Hofman, M. S., Calais, J., Czernin, J., Ilhan, H., Saad, F., Small, E. J., Smith, M. R., et al. (2019) Prostate-Specific Membrane Antigen Ligand Positron Emission Tomography in Men with Nonmetastatic Castration-Resistant Prostate Cancer. *Clin. Cancer Res. 25*, 7448–7454.

(52) Morigi, J. J., Stricker, P. D., van Leeuwen, P. J., Tang, R., Ho, B., Nguyen, Q., Hruby, G., Fogarty, G., Jagavkar, R., Kneebone, A., et al. (2015) Prospective Comparison of ^{18}F-Fluoromethylcholine Versus ^{68}Ga-PSMA PET/CT in Prostate Cancer Patients Who Have Rising PSA After Curative Treatment and Are Being Considered for Targeted Therapy. *J. Nucl. Med. 56*, 1185–90.

(53) Wit, E. M. K., Acar, C., Grivas, N., Yuan, C., Horenblas, S., Liedberg, F., Valdés Olmos, R. A., van Leeuwen, F. W. B., van den Berg, N. S., Winter, A., et al. (2017) Sentinel Node Procedure in Prostate Cancer: A Systematic Review to Assess Diagnostic Accuracy. *Eur. Urol. 71*, 596–605.

(54) Maurer, T., Gschwend, J. E., and Eiber, M. (2018) Prostate-specific membrane antigen-guided salvage lymph node dissection in recurrent prostate cancer: a novel technology to detect lymph node metastases. *Curr. Opin Urol 28*, 191–196.

(55) Jilg, C. A., Drendel, V., Rischke, H. C., Beck, T., Vach, W., Schaal, K., Wetterauer, U., Schultze-Seemann, W., and Meyer, P. T. (2017) Diagnostic Accuracy of Ga-68-HBED-CC-PSMA-Ligand-PET/CT before Salvage Lymph Node Dissection for Recurrent Prostate Cancer. *Theranostics 7*, 1770–1780.

(56) van Leeuwen, F. W., and van der Poel, H. G. (2016) Surgical Guidance in Prostate Cancer: "From Molecule to Man" Translations. *Clin. Cancer Res. 22*, 1304–6.

(57) Horn, T., Kronke, M., Rauscher, I., Haller, B., Robu, S., Wester, H.-J., Schottelius, M., van Leeuwen, F. W. B., van der Poel, H. G., Heck, M., et al. (2019) Single Lesion on Prostate-specific Membrane Antigen-ligand Positron Emission Tomography and Low Prostate-specific Antigen Are Prognostic Factors for a Favorable Biochemical Response to Prostate-specific Membrane Antigen-targeted Radioguided Surgery in Recurrent Prostate Cancer. *Eur. Urol. 76*, 517–523.

(58) Schlomm, T., Tennstedt, P., Huxhold, C., Steuber, T., Salomon, G., Michl, U., Heinzer, H., Hansen, J., Budaus, L., Steurer, S., et al. (2012) Neurovascular structure-adjacent frozen-section examination (Neuro SAFE) increases nerve-sparing frequency and reduces positive surgical margins in open and robot-assisted laparoscopic radical prostatectomy: experience after 11,069 consecutive patients. *Eur. Urol. 62*, 333–40.

(59) Beyer, B., Schlomm, T., Tennstedt, P., Boehm, K., Adam, M., Schiffmann, J., Sauter, G., Wittmer, C., Steuber, T., Graefen, M., et al. (2014) A feasible and time-efficient adaptation of Neuro SAFE for da Vinci robot-assisted radical prostatectomy. *Eur. Urol. 66*, 138–44.

(60) Kratochwil, C., Giesel, F. L., Leotta, K., Eder, M., Hoppe-Tich, T., Youssoufian, H., Kopka, K., Babich, J. W., and Haberkorn, U. (2015) PMPA for nephroprotection in PSMA-targeted radionuclide therapy of prostate cancer. *J. Nucl. Med. 56*, 293–8.

(61) Fendler, W. P., Czernin, J., Herrmann, K., and Beyer, T. (2016) Variations in PET/MRI Operations: Results from an International Survey Among 39 Active Sites. *J. Nucl. Med. 57*, 2016–2021.

(62) Ray Banerjee, S., Pullambhatla, M., Foss, C. A., Falk, A., Byun, Y., Nimmagadda, S., Mease, R. C., and Pomper, M. G. (2013) Effect of chelators on the pharmacokinetics of (99m)Tc-labeled imaging agents for the prostate-specific membrane antigen (PSMA). *J. Med. Chem. 56*, 6108–21.

(63) Ray Banerjee, S., Chen, Z., Pullambhatla, M., Lisok, A., Chen, J., Mease, R. C., and Pomper, M. G. (2016) Preclinical Comparative Study of (68)Ga-Labeled DOTA, NOTA, and HBED-CC Chelated Radiotracers for Targeting PSMA. *Bioconjugate Chem. 27*, 1447–55.

(64) Gourni, E., Canovas, C., Goncalves, V., Denat, F., Meyer, P. T., and Mäcke, H. R. (2015) (R)-NODAGA-PSMA: A Versatile Precursor for Radiometal Labeling and Nuclear Imaging of PSMA-Positive Tumors. *PLoS One 10*, No. e0145755.

(65) Zha, Z., Ploessl, K., Choi, S. R., Wu, Z., Zhu, L., and Kung, H. F. (2018) Synthesis and evaluation of a novel urea-based (68)Ga-complex for imaging PSMA binding in tumor. *Nucl. Med. Biol. 59*, 36–47.

(66) Kiess, A. P., Minn, I., Vaidyanathan, G., Hobbs, R. F., Josefsson, A., Shen, C., Brummet, M., Chen, Y., Choi, J., Koumarianou, E., et al. (2016) (2S)-2-(3-(1-Carboxy-5-(4−211At-Astatobenzamido)Pentyl)-Ureido)-Pentanedioic Acid for PSMA-Targeted alpha-Particle Radiopharmaceutical Therapy. *J. Nucl. Med. 57*, 1569−1575.

(67) Pandit-Taskar, N., O'Donoghue, J. A., Beylergil, V., Lyashchenko, S., Ruan, S., Solomon, S. B., Durack, J. C., Carrasquillo, J. A., Lefkowitz, R. A., Gonen, M., et al. (2014) (89)Zr-huJ591 immuno-PET imaging in patients with advanced metastatic prostate cancer. *Eur. J. Nucl. Med. Mol. Imaging 41*, 2093−105.

(68) Tagawa, S. T., Milowsky, M. I., Morris, M., Vallabhajosula, S., Christos, P., Akhtar, N. H., Osborne, J., Goldsmith, S. J., Larson, S., Taskar, N. P., et al. (2013) Phase II study of Lutetium-177-labeled anti-prostate-specific membrane antigen monoclonal antibody J591 for metastatic castration-resistant prostate cancer. *Clin. Cancer Res. 19*, 5182−91.

(69) Melis, M., Krenning, E. P., Bernard, B. F., Barone, R., Visser, T. J., and de Jong, M. (2005) Localisation and mechanism of renal retention of radiolabelled somatostatin analogues. *Eur. J. Nucl. Med. Mol. Imaging 32*, 1136−43.

(70) Tanner, G. A. (1995) Renal Physiology and Body Fluids. In *Medical Physiology*, 1st ed. (Rhoades, R. A., and Tanner, G. A., Eds.) pp 418−481, Lippincott Williams & Wilkins, Baltimore, MD.

(71) Weyer, K., Nielsen, R., Petersen, S. V., Christensen, E. I., Rehling, M., and Birn, H. (2013) Renal uptake of ^{99m}Tc-dimercaptosuccinic acid is dependent on normal proximal tubule receptor-mediated endocytosis. *J. Nucl. Med. 54*, 159−65.

(72) Eshbach, M. L., and Weisz, O. A. (2017) Receptor-Mediated Endocytosis in the Proximal Tubule. *Annu. Rev. Physiol. 79*, 425−448.

(73) KleinJan, G. H., Bunschoten, A., van den Berg, N. S., Olmos, R. A., Klop, W. M., Horenblas, S., van der Poel, H. G., Wester, H.-J., and van Leeuwen, F. W. (2016) Fluorescence guided surgery and tracer-dose, fact or fiction? *Eur. J. Nucl. Med. Mol. Imaging 43*, 1857−67.

(74) Meershoek, P., KleinJan, G. H., van Oosterom, M. N., Wit, E. M. K., van Willigen, D. M., Bauwens, K. P., van Gennep, E. J., Mottrie, A. M., van der Poel, H. G., and van Leeuwen, F. W. B. (2018) Multispectral-Fluorescence Imaging as a Tool to Separate Healthy from Disease-Related Lymphatic Anatomy During Robot-Assisted Laparoscopy. *J. Nucl. Med. 59*, 1757−1760.

(75) Schottelius, M., Wurzer, A., Wissmiller, K., Beck, R., Koch, M., Gorpas, D., Notni, J., Buckle, T., van Oosterom, M. N., Steiger, K., et al. (2019) Synthesis and Preclinical Characterization of the PSMA-Targeted Hybrid Tracer PSMA-I&F for Nuclear and Fluorescence Imaging of Prostate Cancer. *J. Nucl. Med. 60*, 71−78.

(76) van Leeuwen, F. W. B., van Oosterom, M. N., Meershoek, P., van Leeuwen, P. J., Berliner, C., van der Poel, H. G., Graefen, M., and Maurer, T. (2019) Minimal-Invasive Robot-Assisted Image-Guided Resection of Prostate-Specific Membrane Antigen-Positive Lymph Nodes in Recurrent Prostate Cancer. *Clin Nucl. Med. 44*, 580−581.

(77) Maurer, T., Weirich, G., Schottelius, M., Weineisen, M., Frisch, B., Okur, A., Kubler, H., Thalgott, M., Navab, N., Schwaiger, M., et al. (2015) Prostate-specific membrane antigen-radioguided surgery for metastatic lymph nodes in prostate cancer. *Eur. Urol. 68*, 530−4.

(78) Eder, M., Schäfer, M., Bauder-Wüst, U., Hull, W. E., Wangler, C., Mier, W., Haberkorn, U., and Eisenhut, M. (2012) ^{68}Ga-complex lipophilicity and the targeting property of a urea-based PSMA inhibitor for PET imaging. *Bioconjugate Chem. 23*, 688−97.

(79) Orsaria, P., Chiaravalloti, A., Fiorentini, A., Pistolese, C., Vanni, G., Granai, A. V., Varvaras, D., Danieli, R., Schillaci, O., Petrella, G., et al. (2017) PET Probe-Guided Surgery in Patients with Breast Cancer: Proposal for a Methodological Approach. *In Vivo 31*, 101−110.

(80) Collamati, F. (2019) Annual Congress of the European Association of Nuclear Medicine October 12 − 16, 2019 Barcelona, Spain. *Eur. J. Nucl. Med. Mol. Imaging 46*, 1−952.

(81) Van Oosterom, M. N., Rietbergen, D. D. D., Welling, M. M., Van Der Poel, H. G., Maurer, T., and Van Leeuwen, F. W. B. (2019) Recent advances in nuclear and hybrid detection modalities for image-guided surgery. *Expert Rev. Med. Devices 16*, 711−734.

(82) Fragoso Costa, P, Darr, C, Binse, I, Grootendorst, M, Herrmann, K, Hadaschik, B, and Harke, N (2019) Early Results of Intraoperative ^{68}Ga-PSMA Cerenkov Luminescence Imaging in Radical Prostatectomy. *J. Nucl. Med. 60*, 658.

(83) Bunschoten, A., van den Berg, N. S., Valdés Olmos, R. A., Blokland, J. A. K., and van Leeuwen, F. W. B. (2016) Tracers Applied in Radioguided Surgery. In *Radioguided Surgery* (Herrmann, K., Nieweg, O. E., and Povoski, S. P., Eds.) pp 75−101, Springer International Publishing, Cham.

(84) Dwivedi, D. K., Snehlata, Dwivedi, A. K., Lochab, S. P., Kumar, R., Naswa, N., Sharma, P., Malhotra, A., Bandopadhayaya, G. P., Bal, C., et al. (2011) Radiation exposure to nuclear medicine personnel handling positron emitters from Ge-68/Ga-68 generator. *Indian Journal of Nuclear Medicine 26*, 86−90.

(85) Zhao, Y., Shaffer, T. M., Das, S., Perez-Medina, C., Mulder, W. J., and Grimm, J. (2017) Near-Infrared Quantum Dot and (89)Zr Dual-Labeled Nanoparticles for in Vivo Cerenkov Imaging. *Bioconjugate Chem. 28*, 600−608.

(86) Giesel, F. L., Will, L., Lawal, I., Lengana, T., Kratochwil, C., Vorster, M., Neels, O., Reyneke, F., Haberkon, U., Kopka, K., et al. (2018) Intraindividual Comparison of (18)F-PSMA-1007 and (18)F-DCFPyL PET/CT in the Prospective Evaluation of Patients with Newly Diagnosed Prostate Carcinoma: A Pilot Study. *J. Nucl. Med. 59*, 1076−1080.

(87) Zia, N. A., Cullinane, C., Van Zuylekom, J. K., Waldeck, K., McInnes, L. E., Buncic, G., Haskali, M. B., Roselt, P. D., Hicks, R. J., and Donnelly, P. S. (2019) A Bivalent Inhibitor of Prostate Specific Membrane Antigen Radiolabeled with Copper-64 with High Tumor Uptake and Retention. *Angew. Chem., Int. Ed. 58*, 14991−14994.

(88) Frisch, B., Maurer, T., Okur, A., Weineisen, M., Schottelius, M., Kubler, H., Navab, N., Wester, H.-J., Schwaiger, M., and Eiber, M. (2015) Freehand SPECT for In-111-PSMA-I&T radioguided lymphadenectomy in prostate cancer patients. *J. Nucl. Med. 56*, 157.

(89) Rauscher, I., Maurer, T., Souvatzoglou, M., Beer, A. J., Vag, T., Wirtz, M., Weirich, G., Wester, H.-J., Gschwend, J. E., Schwaiger, M., et al. (2016) Intrapatient Comparison of 111In-PSMA I&T SPECT/CT and Hybrid ^{68}Ga-HBED-CC PSMA PET in Patients With Early Recurrent Prostate Cancer. *Clinical Nuclear Medicine 41*, No. e397-e402.

(90) Schollhammer, R., De Clermont Gallerande, H., Yacoub, M., Quintyn Ranty, M. L., Barthe, N., Vimont, D., Hindie, E., Fernandez, P., and Morgat, C. (2019) Comparison of the radiolabeled PSMA-inhibitor (111)In-PSMA-617 and the radiolabeled GRP-R antagonist (111)In-RM2 in primary prostate cancer samples. *EJNMMI Res. 9*, 52.

(91) Bartholomä, M. D., Louie, A. S., Valliant, J. F., and Zubieta, J. (2010) Technetium and gallium derived radiopharmaceuticals: comparing and contrasting the chemistry of two important radiometals for the molecular imaging era. *Chem. Rev. 110*, 2903−20.

(92) Maresca, K. P., Hillier, S. M., Lu, G. L., Marquis, J. C., Zimmerman, C. N., Eckelman, W. C., Joyal, J. L., and Babich, J. W. (2012) Small molecule inhibitors of PSMA incorporating technetium-99m for imaging prostate cancer: Effects of chelate design on pharmacokinetics. *Inorg. Chim. Acta 389*, 168−175.

(93) Robu, S., Schottelius, M., Eiber, M., Maurer, T., Gschwend, J., Schwaiger, M., and Wester, H.-J. (2017) Preclinical Evaluation and First Patient Application of ^{99m}Tc-PSMA-I&S for SPECT Imaging and Radioguided Surgery in Prostate Cancer. *J. Nucl. Med. 58*, 235−242.

(94) Vallabhajosula, S., Nikolopoulou, A., Babich, J. W., Osborne, J. R., Tagawa, S. T., Lipai, I., Solnes, L., Maresca, K. P., Armor, T., Joyal, J. L., et al. (2014) ^{99m}Tc-labeled small-molecule inhibitors of prostate-specific membrane antigen: pharmacokinetics and biodistribution studies in healthy subjects and patients with metastatic prostate cancer. *J. Nucl. Med. 55*, 1791−8.

(95) Xu, X., Zhang, J., Hu, S., He, S., Bao, X., Ma, G., Luo, J., Cheng, J., and Zhang, Y. (2017) (99m)Tc-labeling and evaluation of a HYNIC modified small-molecular inhibitor of prostate-specific membrane antigen. *Nucl. Med. Biol. 48*, 69−75.

(96) Maurer, T., Robu, S., Schottelius, M., Schwamborn, K., Rauscher, I., van den Berg, N. S., van Leeuwen, F. W. B., Haller, B., Horn, T., Heck,

M. M., et al. (2019) (99m)Technetium-based Prostate-specific Membrane Antigen-radioguided Surgery in Recurrent Prostate Cancer. *Eur. Urol. 75*, 659−666.

(97) van Leeuwen, F. W. B., Hardwick, J. C. H., and van Erkel, A. R. (2015) Luminescence-based Imaging Approaches in the Field of Interventional Molecular Imaging. *Radiology 276*, 12−29.

(98) Sengupta, S., Krishnan, M. A., Pandit, A., Dudhe, P., Sharma, R., and Chelvam, V. (2019) Tyrosine-based asymmetric urea ligand for prostate carcinoma: Tuning biological efficacy through in silico studies. *Bioorg. Chem. 91*, 103154.

(99) Wang, X., Huang, S. S., Heston, W. D., Guo, H., Wang, B. C., and Basilion, J. P. (2014) Development of targeted near-infrared imaging agents for prostate cancer. *Mol. Cancer Ther. 13*, 2595−606.

(100) Chen, Y., Chatterjee, S., Lisok, A., Minn, I., Pullambhatla, M., Wharram, B., Wang, Y., Jin, J., Bhujwalla, Z. M., Nimmagadda, S., et al. (2017) A PSMA-targeted theranostic agent for photodynamic therapy. *J. Photochem. Photobiol., B 167*, 111−116.

(101) Chen, Y., Pullambhatla, M., Banerjee, S. R., Byun, Y., Stathis, M., Rojas, C., Slusher, B. S., Mease, R. C., and Pomper, M. G. (2012) Synthesis and biological evaluation of low molecular weight fluorescent imaging agents for the prostate-specific membrane antigen. *Bioconjugate Chem. 23*, 2377−85.

(102) Kwon, Y. D., Chung, H. J., Lee, S. J., Lee, S. H., Jeong, B. H., and Kim, H. K. (2018) Synthesis of novel multivalent fluorescent inhibitors with high affinity to prostate cancer and their biological evaluation. *Bioorg. Med. Chem. Lett. 28*, 572−576.

(103) Kwon, Y. D., Oh, J. M., La, M. T., Chung, H. J., Lee, S. J., Chun, S., Lee, S. H., Jeong, B. H., and Kim, H. K. (2019) Synthesis and Evaluation of Multifunctional Fluorescent Inhibitors with Synergistic Interaction of Prostate-Specific Membrane Antigen and Hypoxia for Prostate Cancer. *Bioconjugate Chem. 30*, 90−100.

(104) Matsuoka, D., Watanabe, H., Shimizu, Y., Kimura, H., Ono, M., and Saji, H. (2017) Synthesis and evaluation of a novel near-infrared fluorescent probe based on succinimidyl-Cys-C(O)-Glu that targets prostate-specific membrane antigen for optical imaging. *Bioorg. Med. Chem. Lett. 27*, 4876−4880.

(105) Bao, K., Lee, J. H., Kang, H., Park, G. K., El Fakhri, G., and Choi, H. S. (2017) PSMA-targeted contrast agents for intraoperative imaging of prostate cancer. *Chem. Commun. (Cambridge, U. K.) 53*, 1611−1614.

(106) Laydner, H., Huang, S. S., Heston, W. D., Autorino, R., Wang, X., Harsch, K. M., Magi-Galluzzi, C., Isac, W., Khanna, R., Hu, B., et al. (2013) Robotic real-time near infrared targeted fluorescence imaging in a murine model of prostate cancer: a feasibility study. *Urology 81*, 451−6.

(107) Shallal, H. M., Minn, I., Banerjee, S. R., Lisok, A., Mease, R. C., and Pomper, M. G. (2014) Heterobivalent agents targeting PSMA and integrin-$\alpha_v\beta_3$. *Bioconjugate Chem. 25*, 393−405.

(108) Kularatne, S. A., Thomas, M., Myers, C. H., Gagare, P., Kanduluru, A. K., Crian, C. J., and Cichocki, B. N. (2019) Evaluation of Novel Prostate-Specific Membrane Antigen-Targeted Near-Infrared Imaging Agent for Fluorescence-Guided Surgery of Prostate Cancer. *Clin. Cancer Res. 25*, 177−187.

(109) van der Wal, S., Kuil, J., Valentijn, A. R. P. M., and van Leeuwen, F. W. B. (2016) Synthesis and systematic evaluation of symmetric sulfonated centrally C−C bonded cyanine near-infrared dyes for protein labelling. *Dyes Pigm. 132*, 7−19.

(110) Van Leeuwen, F. W. B., Schottelius, M., Brouwer, O. R., Vidal-Sicart, S., Achilefu, S., Klode, J., Wester, H.-J., and Buckle, T. (2019) Trending: Radioactive and fluorescent bimodal/hybrid tracers as multiplexing solutions for surgical guidance. *J. Nucl. Med.*, 1.

(111) Banerjee, S. R., Pullambhatla, M., Byun, Y., Nimmagadda, S., Foss, C. A., Green, G., Fox, J. J., Lupold, S. E., Mease, R. C., and Pomper, M. G. (2011) Sequential SPECT and optical imaging of experimental models of prostate cancer with a dual modality inhibitor of the prostate-specific membrane antigen. *Angew. Chem., Int. Ed. 50*, 9167−70.

(112) Garanger, E., Aikawa, E., Reynolds, F., Weissleder, R., and Josephson, L. (2008) Simplified syntheses of complex multifunctional nanomaterials. *Chem. Commun.* No. 39, 4792−4794.

(113) Baranski, A. C., Schäfer, M., Bauder-Wüst, U., Roscher, M., Schmidt, J., Stenau, E., Simpfendorfer, T., Teber, D., Maier-Hein, L., Hadaschik, B., et al. (2018) PSMA-11-Derived Dual-Labeled PSMA Inhibitors for Preoperative PET Imaging and Precise Fluorescence-Guided Surgery of Prostate Cancer. *J. Nucl. Med. 59*, 639−645.

(114) Hensbergen, A. W., Buckle, T., van Willigen, D. M., Schottelius, M., Welling, M. M., van der Wijk, F. A., Maurer, T., van der Poel, H. G., van der Pluijm, G., and van Weerden, W. M. (2019) Hybrid Tracers Based on Cyanine Backbones Targeting Prostate-Specific Membrane Antigen - Tuning Pharmacokinetic Properties and Exploring Dye-Protein Interaction. *J. Nucl. Med.*, 1.

(115) Kommidi, H., Guo, H., Nurili, F., Vedvyas, Y., Jin, M. M., McClure, T. D., Ehdaie, B., Sayman, H. B., Akin, O., Aras, O., et al. (2018) (18)F-Positron Emitting/Trimethine Cyanine-Fluorescent Contrast for Image-Guided Prostate Cancer Management. *J. Med. Chem. 61*, 4256−4262.

(116) Gotthardt, M., van Eerd-Vismale, J., Oyen, W. J., de Jong, M., Zhang, H., Rolleman, E., Mäcke, H. R., Behe, M., and Boerman, O. (2007) Indication for different mechanisms of kidney uptake of radiolabeled peptides. *J. Nucl. Med. 48*, 596−601.

(117) Chatalic, K. L. S., Heskamp, S., Konijnenberg, M., Molkenboer-Kuenen, J. D. M., Franssen, G. M., Clahsen-van Groningen, M. C., Schottelius, M., Wester, H.-J., van Weerden, W. M., Boerman, O. C., et al. (2016) Towards Personalized Treatment of Prostate Cancer: PSMA I&T, a Promising Prostate-Specific Membrane Antigen-Targeted Theranostic Agent. *Theranostics 6*, 849−861.

(118) Wurzer, A., Pollmann, J., Schmidt, A., Reich, D., Wester, H.-J., and Notni, J. (2018) Molar Activity of Ga-68 Labeled PSMA Inhibitor Conjugates Determines PET Imaging Results. *Mol. Pharmaceutics 15*, 4296−4302.

(119) Wagner, C. C., and Langer, O. (2011) Approaches using molecular imaging technology − use of PET in clinical microdose studies. *Adv. Drug Delivery Rev. 63*, 539−46.

(120) Barth, C. W., and Gibbs, S. L. (2017) Direct Administration of Nerve-Specific Contrast to Improve Nerve Sparing Radical Prostatectomy. *Theranostics 7*, 573−593.

(121) Sevick-Muraca, E. M., Sharma, R., Rasmussen, J. C., Marshall, M. V., Wendt, J. A., Pham, H. Q., Bonefas, E., Houston, J. P., Sampath, L., Adams, K. E., et al. (2008) Imaging of Lymph Flow in Breast Cancer Patients after Microdose Administration of a Near-Infrared Fluorophore: Feasibility Study. *Radiology 246*, 734−741.

(122) Gambhir, S. S., Shankar, L. K., Rosenthal, E., Warram, J. M., Ghesani, M., Hope, T. A., Jacobs, P. M., Jacobson, G. B., Wilson, T., and Siegel, B. A. (2019) Proceedings: Pathways for Successful Translation of New Imaging Agents and Modalities-Phase III Studies. *J. Nucl. Med. 60*, 736−744.

(123) Grischke, E. M., Rohm, C., Hahn, M., Helms, G., Brucker, S., and Wallwiener, D. (2015) ICG Fluorescence Technique for the Detection of Sentinel Lymph Nodes in Breast Cancer: Results of a Prospective Open-label Clinical Trial. *Geburtshilfe Frauenheilkd. 75*, 935−940.

(124) van den Bos, J., Wieringa, F. P., Bouvy, N. D., and Stassen, L. P. S. (2018) Optimizing the image of fluorescence cholangiography using ICG: a systematic review and ex vivo experiments. *Surgical Endoscopy 32*, 4820−4832.

(125) Chatalic, K. L., Veldhoven-Zweistra, J., Bolkestein, M., Hoeben, S., Koning, G. A., Boerman, O. C., de Jong, M., and van Weerden, W. M. (2015) A Novel (111)In-Labeled Anti-Prostate-Specific Membrane Antigen Nanobody for Targeted SPECT/CT Imaging of Prostate Cancer. *J. Nucl. Med. 56*, 1094−9.

(126) Pandit-Taskar, N., O'Donoghue, J. A., Morris, M. J., Wills, E. A., Schwartz, L. H., Gonen, M., Scher, H. I., Larson, S. M., and Divgi, C. R. (2008) Antibody mass escalation study in patients with castration-resistant prostate cancer using 111In-J591: lesion detectability and dosimetric projections for ^{90}Y radioimmunotherapy. *J. Nucl. Med. 49*, 1066−74.

(127) Psimadas, D., Valotassiou, V., Alexiou, S., Tsougos, I., and Georgoulias, P. (2018) Radiolabeled mAbs as Molecular Imaging and/or Therapy Agents Targeting PSMA. *Cancer Invest. 36*, 118−128.

(128) Taneja, S. S. (2004) Imaging in the diagnosis and management of prostate cancer. *Rev. Urol 6*, 101−13.

(129) Lütje, S., Rijpkema, M., Franssen, G. M., Fracasso, G., Helfrich, W., Eek, A., Oyen, W. J., Colombatti, M., and Boerman, O. C. (2014) Dual-Modality Image-Guided Surgery of Prostate Cancer with a Radiolabeled Fluorescent Anti-PSMA Monoclonal Antibody. *J. Nucl. Med. 55*, 995−1001.

(130) Loktev, A., Lindner, T., Mier, W., Debus, J., Altmann, A., Jager, D., Giesel, F., Kratochwil, C., Barthe, P., Roumestand, C., et al. (2018) A Tumor-Imaging Method Targeting Cancer-Associated Fibroblasts. *J. Nucl. Med. 59*, 1423−1429.

(131) Ananias, H. J., de Jong, I. J., Dierckx, R. A., van de Wiele, C., Helfrich, W., and Elsinga, P. H. (2008) Nuclear imaging of prostate cancer with gastrin-releasing-peptide-receptor targeted radiopharmaceuticals. *Curr. Pharm. Des. 14*, 3033−47.